Eindhoven University of Technology

MASTER

Ideal magnetohydrodynamics based filter for tearing mode prediction on the DIII-D tokamak

Roelofs, M.A.

Award date:
2018

Link to publication

Disclaimer
This document contains a student thesis (bachelor's or master's), as authored by a student at Eindhoven University of Technology. Student theses are made available in the TU/e repository upon obtaining the required degree. The grade received is not published on the document as presented in the repository. The required complexity or quality of research of student theses may vary by program, and the required minimum study period may vary in duration.

General rights
Copyright and moral rights for the publications made accessible in the public portal are retained by the authors and/or other copyright owners and it is a condition of accessing publications that users recognise and abide by the legal requirements associated with these rights.

- Users may download and print one copy of any publication from the public portal for the purpose of private study or research.
- You may not further distribute the material or use it for any profit-making activity or commercial gain

Technische Universiteit
Eindhoven
University of Technology

Science and Technology of Nuclear Fusion
Mechanical Engineering

Ideal magnetohydrodynamics based filter for tearing mode prediction on the DIII-D tokamak

Graduation Thesis

M.A. Roelofs

Supervisors:
F.A.A. Felici - *Eindhoven University of Technology*
E. Kolemen - *Princeton University*
N.J. Lopes Cardozo - *Eindhoven University of Technology*

Eindhoven, 2018

Abstract

An algorithm has been developed to predict that start of tearing modes that end up having a root-mean-square (RMS) bigger than 26 by looking at the increase of the standard deviation of ideal MHD stability. A code has been developed, CAKE, that is able to generate a large amount of plasma equilibria that show important physical features such as the pedestal. These 'kinetic equilibria' can be generated in tens of seconds instead of hours, making it possible to do statistical analysis of experimental data. To see if it is possible to predict tearing modes by looking at the standard deviation of ideal MHD stability, unscented transform is applied. Using a method comparable to Monte-Carlo simulations, it is possible to determine the standard deviation of ideal MHD stability by perturbing the input data by CAKE with a deterministic amount and compute the ideal MHD stability for all these cases. From this, the mean and standard deviation of the ideal MHD stability can be calculated. Due to the presence of noise in the calculations, a filter has been applied. This makes it possible to get a more accurate result by filtering out noise. An unscented Kalman filter has been picked for this purpose due to its ability to work with non-linear systems and the fact that the standard deviation is a product of the filter and not an input. Filtering three high discharges with a high temporal resolution shows that it is possible to filter out some of the noise, resulting in a more clear result. It however does not improve the predictability capability since the tearing modes still need to have an RMS that is bigger than 26 to be able to be detected this way.

Contents

Chapter 1

Introduction

Nuclear fusion as an energy source sounds like something from a science-fiction novel. However, it is not unreasonable to assume that fusion power might be a commercial product within 70 years. Before we are at that stage, still a lot of works needs to be done since there are still unsolved challenges. But before we discuss some of these challenges an overview of nuclear fusion is given first.

The biggest, and probably most well known fusion process, is the sun [1]. The energy that gets released by the sun, and what we experience as heat and light, is the by-product of the fusion process that is going on in its core. Due to the very large mass of the sun hydrogen particles, that make up the bulk of the sun's material, are not able to escape. Instead they are fused together, creating helium and releasing energy in the process.

A nuclear fusion power plant tries to mimic the behavior by fusing two isotopes of hydrogen particles, deuterium and tritium, into a helium particle and a neutron. If the kinetic energy of the neutron particle can be conversed to heat and captured together with the heat produced by the process it will be possible to power, for example, a steam cycle to generate electricity. While this is a technological challenge by itself, due to the large amounts of energy in play, maintaining a stable fusion plasma on Earth is a challenge by itself[2].

Various types of fusion process can be distinguished. For example, fusion by gravity, is what happens in the sun and other starts. Due to the huge mass the gravitational pull of the sun is so large that the bulk of particles does not escape. Instead, they are forced together and as a result the particles fuse. This type of fusion is not possible on Earth, because it would take more mass that anything on the Earth combined. A second type of fusion is called 'inertial confinement fusion'. This type of fusion generates fusion by firing a high-energy beam on a fuel pellet, heating and compressing it as a result[3]. A third type is fusion due to magnetic confinement. By forcing the charged particles that makes up the plasma to follow magnetic field lines, they will travel a very long distance and as a result increase the amount that particles will collide and fuse[3]. This method currently looks best for a commercial fusion power plant.

A magnetic confined plasma has the risk of disrupting. While the theory of ideal magnetohydrodynamics (MHD) is well understood and gives a clear overview of the physical limits, predicting and detecting the on-set of ideal MHD instabilities is very important for commercial tokamaks and even ITER.

1.1 Motivation and research goal

Many engineering and physics challenges need to be solved before commercial fusion is achieved, getting a better understanding of plasma stability being one of them.

Plasma instabilities have a range of effects, from benign phenomena such as sawteeth [3, 4], to a complete disruption. During a disruption all the plasma energy gets deposited on the first wall, which can damage a small reactor but is catastrophic on larger machines [5, 2]. A theoretical framework to study plasma stability is ideal magnetohydrodynamics (MHD) [6, 7]. MHD is the study of charged fluids, resulting in a combination of fluid mechanics and electrodynamics. Ideal MHD assumes that the resistivity in the plasma is negligible which results in the boundary conditions that the magnetic field lines are 'frozen'.

The frozen field lines concept means that perpendicular to the magnetic field lines the field lines do not move with regard to the plasma and limits the scope of possible plasma instabilities [6]. However, the instabilities that can occur are considered much more dangerous since these effects are global instead of local and due to the fast time scales on which they occur [8]. Modern control systems in tokamaks are able to detect a large range of instabilities and are able to suppress them, but prediction to prevent them altogether is still an active field of work [9, 10, 11].

Special interest is for the so-called 'tearing modes'[12, 13]. These can be understood when studying resistive MHD, in which the field lines are not frozen[14]. These tearing modes degrade the performance of the fusion plasma in the best case and in worst case they can cause a disruption. Since tearing modes are primarily driven by the pressure gradient, which is a parameter that one wants to increase as much as possible for high performance fusion plasmas, preventing tearing modes while having a high pressure is paramount in operating a successful commercial fusion reactor[3].

While theory shows a clear distinction between resistive and ideal MHD work by, for example, Brennan et al[8, 15] have shown that there is a correlation between the two. In this work it has been shown that tearing modes develop easier near the ideal stability limits and so one could wonder if ideal MHD can be used to predict the onset of tearing modes, without studying resistive MHD.

Quantifying the stability of the plasma, can be done by studying the ideal MHD energy principle [16, 2]. This calculates if there are any perturbations of the plasma that would result in a lower energy state. As a result we can state that if such a perturbation exists, the plasma is unstable. To be able to perform this calculation, which can done using the 'DCON'-code [17] for example, important data about the state of the plasma needs to be determined: the plasma equilibrium.

The plasma equilibrium refers to the force balance in the plasma [2]. The outward force caused by the pressure gradient of the plasma needs to be equal to the inward Lorentz-force due to the plasma current and the magnetic field. The solution makes it possible to study pressure and current density locally in the plasma, which is extremely useful for all kinds of plasma analysis, including ideal MHD studies.

Solving the plasma equilibrium remains a difficult task since local data about the pressure and current density is needed to find a solution. Traditionally only data from magnetics are being used, but this lacks overall accuracy [18]. However, using additional diagnostics it is possible to enhance the accuracy of the reconstructed plasma equilibrium.

For this, a new code is developed, improving on the magnetics-only reconstruction by taking measurements from Thomson Scattering (TS), Charge Exchange Recombination (CER) and the Motional Stark Effect (MSE) in to account. This results in so-called kinetic equilibrium, hence the codes name: Consistent Automatic Kinetic Equilibrium (CAKE) [19].

The output from DCON is a single number and does not provide any estimate of its uncertainty.

It is known that there is an uncertainty on the measurement data used to reconstruct the plasma equilibrium so it is safe to assume that there is a non-negligible uncertainty on the output of DCON. One way of obtaining the uncertainty is using 'unscentend transform' [20]. The major advantage of using this technique is because of its speed, it needs significantly less computations than similar techniques such as Monte-Carlo simulations to converge to a solution.

It will be shown that for a subset of discharges that end in a tearing mode, the start of these tearing modes can be predicted when the uncertainty of the output of DCON is studied as a function of time. Due to the presence of noise in the calculation of the uncertainty and a lack in quality of data for some time slices, the result is being filtered. This removes some of the noise and it causes the calculation of the uncertainty to be more robust against corrupt data due to the inclusion of a model.

The dynamics of this system would be highly non-linear and would have diagnostic data as inputs and the uncertainty of the DCON output as its output. Due to the non-linearity of the system an unscented Kalman filter will be used to filter the data [21]. The Kalman filter is a recursive filter that can be used to estimate the state of a linear system. This can be extended to an unscented Kalman filter, which is also able to process non-linear system and does not need the variances of the process or measurement noise as an input.

A schematic overview that depicts the whole process, from discharge data generated by the experiment to the output of DCON, can be found in figure 1.1

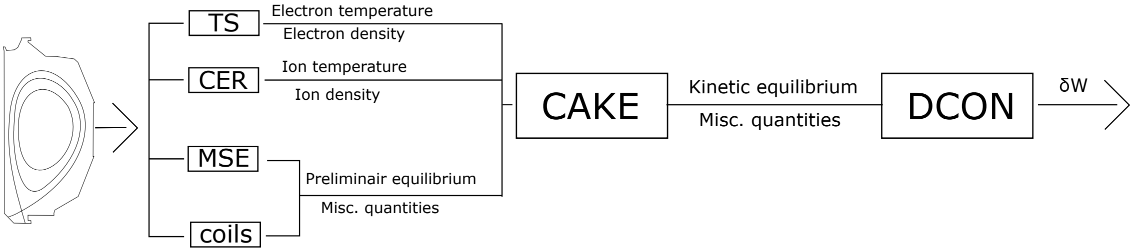

Figure 1.1: Schematic overview of envisioned workflow. Information is gathered from the DIII-D, using 4 types of diagnostics. This data gets used to reconstruct an equilibrium using the CAKE code. This data can be used to look at the ideal MHD plasma stability using DCON and studying δW.

1.1.1 Research question

The main goal of this project is to see if it is possible to develop an algorithm that predicts tearing modes by looking at ideal MHD only. To do this the following research questions have been posed:

Is it possible to predict the start of a tearing mode by calculating the uncertainty of ideal magnetohydrodynamic calculations?

This can be answered after the following subquestions have been answered:

- *Does the Consistent Automatic Kinetic Equilibrium (CAKE) solver provides accurate kinetic equilibria?*
- *Can the uncertainty be determined of the ideal magnetohydrodynamic stability calculation results from 'DCON'?*

Chapter 2 will give a theoretical background necessary for the rest of this work. The Grad-Shafranov equation, which is at the basis of equilibrium reconstruction, will be discussed. Next, an introduction to ideal MHD stability will be given and a connection to non-ideal MHD stability is introduced. The last part of the chapter talks about filter design and the estimation of uncertainty through 'unscented transform'.

Chapter 3 discusses the various codes that are being used as well as well as the nuclear fusion experiment the data is taken from and important diagnostics. First, the DIII-D reactor will be introduced as well as the most important diagnostics for this work: Thomson Scattering (TS), Charge Exchange Recombination (CER) and Motional Stark Effect (MSE). After that the code that will be used to reconstruct the plasma equilibrium, CAKE, will be introduced. It will be explained how the validity of the results are verified. An introduction to DCON will be given next, and two examples will be given. The chapter concludes with looking how the various diagnostics affect the results from DCON.

Chapter 4 applies unscented transform to determine the uncertainty of the DCON results. The algorithm will be discussed, including a discussion about the effect of noise and the scaling of free parameters that are introduced in the algorithm. Next, a filter will be designed. A brief discussion is present about a model, as well as an example to show that the algorithm is working as intended. It is applied to three discharges that have a high temporal resolution.

The results of this work be discussed in chapter 5. This chapter will reflect on the posed research questions and the final result while giving suggestions for further work.

Chapter 2

Literature Study

The detection algorithm that is being designed has its foundation in four different parts of theory: the Grad-Shafranov equation, ideal magnetohydrodynamic (MHD) stability, the Kalman filter and unscented transform. The Grad-Shafranov equation makes it possible to calculate the plasma equilibrium if ideal MHD is assumed. For this flux surfaces are being introduced. Ideal MHD stability is studied from the energy principle theory. A subsection is introduced afterwards that shows a connection between ideal stability limits and the start of tearing modes.

Next, two techniques from control engineering are being introduced: the Kalman filter and unscented transform. The Kalman filter is a way of combining measurement data and a model to estimate the internal state with the least possible covariance. For this to be applied, uncertainty from data needs to be known. Since this is not the case in this work, unscented transform is introduced to determine the output uncertainty. These techniques can be combined in to the 'unscented Kalman filter', which is the filter that will be used as part of the detection algorithm.

2.1 Grad-Shafranov Equation

Summary: Grad-Shafranov Equation

The Grad-Shafranov equation is the solution for a force balance equation in a Tokamak or the 'plasma equilibrium' if the plasma resistivity is assumed to be negligible and a steady-state situation is assumed. The inward Lorentz-force, as a result of the plasma current and the magnetic field, needs to be equal to the outward force caused by the pressure gradient in the plasma. The challenge in solving this equation is due to the switching from Carthesian coordinates to 'flux-surface' coordinates. This equation is at the basis of the equilibrium reconstruction code CAKE and is therefore very important.

One of the most important physical phenomena for this thesis is the force balance in the plasma. The force balance states that the inward force caused by the product of the current and magnetic field needs to be equal to the outward force caused by the pressure gradient of the plasma. Studying this behavior but for tokamak relevant shapes can be done using the Grad-Shafranov equation [22]. Before this equation is derived, flux surfaces need to be introduced.

2.1.1 Flux surfaces

When studying a tokamak, it is often done from the perspective of a flux surface. A flux surface is defined as a surface where holds that:

$$\boldsymbol{B} \cdot \boldsymbol{n} = 0 \tag{2.1}$$

In this equation, $\boldsymbol{B}$ is the magnetic field and $\boldsymbol{n}$ is the normal on a surface. In other words, the flux surface is defined as an area where the magnetic field is constant. Equation 2.1 can be extended by including a 'flux function" f. The resulting equation than becomes:

$$\boldsymbol{B} \cdot \boldsymbol{\nabla} f = 0 \tag{2.2}$$

When considering the flux surfaces inside a tokamak, often the ideal image of an organized and nested structure is considered. When studying these nested structures, it is important to keep track of 'q-surfaces'. These q-surfaces can be described as the ratio between toroidal and poloidal windings of the magnetic field lines. This can be described by:

$$q(\psi) = \frac{1}{2\pi} \oint \frac{1}{RB_\phi |\nabla \psi|} dl \tag{2.3}$$

In this equation, l is the circumference of the q-surface, R is the distance from the midpoint of the tokamak to the q-surface and ψ is the magnetic flux function. This flux function will be discussed and derived in a later section. This can by approximated by equation 2.4 if the location of the last closed flux surface is known.

$$q(r) = \frac{m}{n} = \frac{rB_\phi(r)}{R_0 B_\theta(r)} \tag{2.4}$$

In this equation, m is the poloidal mode number, n the toroidal mode number, r the minor radius, B_t the toroidal magnetic field, R_0 the major radius and B_θ the poloidal magnetic field.

2.1.2 Grad-Shafranov equation

When studying either the plasma stability, information is needed about the plasma equilibrium. To reconstruct the plasma equilibrium one has to solve the Grad-Shafranov equation (GSE).

The GSE can be derived by looking at the MHD force balance of a plasma in a tokamak. The magnetic field combined with a current causes an inward force on the plasma, while the plasma itself has an outward pressure gradient. This can be seen in equation 2.5.

$$\boldsymbol{j} \times \boldsymbol{B} = \nabla p \tag{2.5}$$

When solving this equation for a tokamak plasma, it is assumed that the plasma is toroidally symmetric. When studying the plasma in cylindrical coordinates, the set of equations is reduced to two dimensions: R and Z.

To solve the equation for a tokamak, the magnetic field in the poloidal ($\boldsymbol{B_\theta}$) direction needs to be written in components of a scalar function. This can be done by introducing the magnetic flux function:

$$\psi(R, Z) = \int \boldsymbol{B}_\theta dS \tag{2.6}$$

Surface S is denoted in figure 2.1.

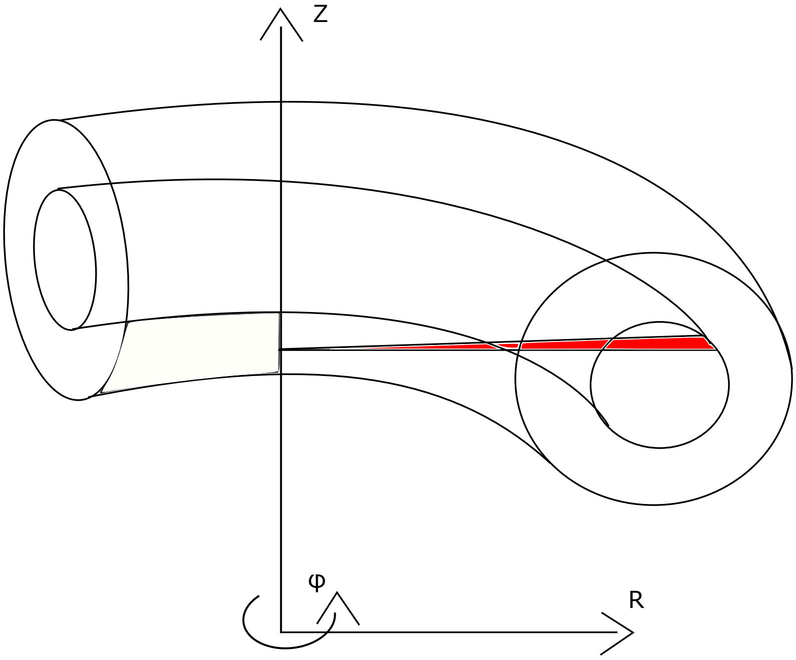

Figure 2.1: The flux surface as defined for this work.

Starting from equation 2.5 it is possible to derive the Grad-Shafranov equation (GSE):

$$\Delta^* \psi = -\mu_0 R^2 P' - FF' \tag{2.7a}$$

This equation is made up out of the elliptic operator $\Delta^*\psi$, as defined in equation 2.8, the pressure P and $F = RB_\phi$. The prime denotes the derivative to ψ.

$$\Delta^*\psi \equiv \frac{\partial^2\psi}{\partial Z^2} + R\frac{\partial}{\partial R}\left(\frac{1}{R}\frac{\partial\psi}{\partial R}\right) \tag{2.8}$$

The GSE is the main equation that is being solved by equilibrium reconstruction tools such as the EFIT code. Using measurement data from various diagnostics, it is possible to solve the above equation. Doing so results in the pressure and current density as a function of $\psi(R, Z)$, two very important plasma properties for studying ideal MHD stability.

2.2 Ideal magnetohydrodynamic stability

Summary: Ideal MHD stability

Ideal MHD assumes that there is a negligible amount of resistivity in the plasma. This assumption has a large impact on the plasma behavior: it makes it impossible for magnetic fields lines to reconnect. Ideal MHD stability can be studied from an energy principle. By looking at δW, the energy gain that is needed to achieve a different plasma shape, the plasma can be virtually perturbed and stability can be studied. A negative δW would mean that there is at least one perturbation that results in the plasma achieving a more energy favorable state. In this case we state that the plasma is ideal MHD unstable. A positive value for δW means the opposite: the plasma is ideal stable for all perturbations. The subsection is concluded with a comparison of resistive MHD stability and how it is effected by the presence of ideal stability limits. A much seen resistive ideal MHD instability is the so-called 'tearing mode'. Due to the reconnecting of the magnetic field lines, island shapes are present in the plasma resulting in a significant loss of performance and can even result in disruptions of the plasma.

The ideal MHD[6, 3] model assumes that there is a negligible amount of resistivity resulting in a perfect conductor. This results in the ideal system with nested flux surfaces with frozen field lines. Frozen field linies means that perpendicular to the magnetic field lines the field lines do not move with regard to the plasma.

This also explains why tearing modes[12, 14, 7] are not possible to study using ideal MHD. For a tearing mode field lines need to be able to reconnect in the plasma and this can't happen if they are frozen[13]. Instabilities caused by reconnection usually act on a much slower timescale compared to ideal MHD and are often local, opposed to ideal MHD stabilities[2]. As a result, the general consensus is that ideal MHD is considered to be a much more 'dangerous' type of instabilities and must be avoided at all cost.

2.2.1 Ideal MHD: energy principle

The one fluid model that can be used to describe an ideal MHD plasma is a combination of fluid dynamics (conservation laws) and electrodynamics. These eight equations are:

$$\frac{d\rho}{dt} + \rho\nabla\cdot\mathbf{v} = 0 \tag{2.9a}$$

$$\frac{d}{dt}\left(\frac{p}{p^{\gamma}}\right) = 0 \tag{2.9b}$$

$$\rho\frac{d\mathbf{v}}{dt} = \mathbf{J}\times\mathbf{B} - \nabla p \tag{2.9c}$$

$$\mathbf{E} + \mathbf{v}\times\mathbf{B} = 0 \tag{2.9d}$$

$$\nabla\times\mathbf{E} = -\frac{\partial\mathbf{B}}{\partial t} \tag{2.9e}$$

$$\nabla\times\mathbf{B} = \mu_0\mathbf{J} \tag{2.9f}$$

$$\nabla\cdot\mathbf{B} = 0 \tag{2.9g}$$

These equations can be combined in to a so-called 'energy principle'. Doing so, it will be possible to study what happens to the total stored plasma energy (W) if the plasma is perturbed. We state that a positive δW is a necessary and sufficient condition to state the the plasma is stable for all perturbations ξ[6]. A negative value indicate that the plasma is unstable for at least one perturbation. Equation 2.10 shows this equation for a tokamak plasma.

$$\delta W = \frac{1}{2}\int \frac{|\boldsymbol{Q}_\perp|^2}{\mu_0} + \frac{B_0^2}{\mu_0}|\nabla\cdot\xi_\perp + 2\xi_\perp + \boldsymbol{\kappa}|^2 + \gamma p_0|\nabla\cdot\xi|^2 - 2(\xi_\perp - \nabla p_0)(\boldsymbol{\kappa}\xi_\perp^*) - J_{0\perp}(\xi_\perp^* \times \boldsymbol{b})\cdot\boldsymbol{Q}_\perp d\boldsymbol{r} \tag{2.10}$$

In this equation $\boldsymbol{\kappa} = \nabla\cdot\boldsymbol{b}$, $\boldsymbol{b}$ is the field line curvature, $\boldsymbol{Q}$ is the magnetic field line bending energy. Looking at the five different terms of the equation, it can be seen that the first three terms are positive and are stabilizing terms while the last two terms are destabilizing terms.

The first destabilizing term, $-2(\xi_\perp - \nabla p_0)(\boldsymbol{\kappa}\xi_\perp^*)$, scales with ∇p_0. As a result, we can state that this term causes the pressure driven instabilities. The most important pressure driven instabilities are the interchange mode and the ballooning mode.

The second destabilizing term, $J_{0\perp}(\xi_\perp^* \times \boldsymbol{b})\cdot\boldsymbol{Q}_\perp$ is proportional to $\boldsymbol{J_0}$, and captures the current driven instabilities. It is the cause of the kink instabilities, which is made up out of the internal and external kind mode [3].

Internal kink modes assume that the boundary of the plasma is fixed. As a result, the kink deformation happens inside the plasma. One example of an internal kink mode is the sawtoothing of the plasma if $q_{min} < 1$. This is a rather harmless process, and is considered to be an important way of removing helium particles from the plasma.

More dangerous is the external kink mode, due to the changing of the boundary of the plasma. To determine if the plasma has an external kink mode, it is not sufficient to study equation 2.10. The presence of a vacuum around the plasma, which allows the edge boundary to deform in the first place, has a stabilizing effect. The relation to calculate the 'total' δW is a linear one: $\delta W_T = \delta W_p + \delta W_v$[23]. It can be found by adding the contribution of the vacuum (δW_v) to equation 2.10. As a result, we can state that if there is a perturbation that causes the plasma to have an external kink mode, the plasma is also unstable to internal kink modes. However, this does not hold the other way around.

Studying a plasma from a theoretical point of view as done in this subsection is fundamental to understanding what can happen with a plasma. However, the clear distinction between pressure and current driven instabilities are hardly seen in experiments [2].

The ideal stability of the plasma will be calculated using the DCON code. As input, a calculated equilibrium is needed. DCON is then able to determine δW of the fusion plasma.

2.2.2 Tearing modes near ideal stability limits

The onset of a tearing mode is thoroughly studied, but especially in high β and highly shaped plasma not yet fully understood. Ideal modes, such as sawteeth and edge localized modes (ELMs), are thought to cause forced reconnection [8]. A distinction can be made between classical tearing modes and neoclassical tearing modes (NTMs).

Furth et al [24] proposed a linear tearing stability index, Δ', which indicates that a classical tearing mode is growing when it is positive. However, it has been witnessed experimentally that tearing modes appear even when Δ' is negative. These are the NTMs, and it has been assumed that their growth is triggered by the seeding of an ideal mode.

Work by Brennan et al [15] proposes an alternative mechanism which is not incompatible with the forced reconnection theory described above. Brennan argues that the if the plasma is near an ideal MHD stability limit, the value for Δ' becomes very sensitive to perturbations in the plasma equilibrium. This is theory is the driving idea behind this work: does the opposite also hold? Does ideal MHD stability analysis becomes very sensitive to perturbations if the plasma approaches a tearing mode?

2.3 Kalman filter

Physicist Summary: Kalman filtering

In control engineering, it is important to know the state of the system, which can be difficult due to the presence of process noise and measurement noise. A much used algorithm to do this the Kalman filter. A Kalman filter looks, using a least-squares like approach, at what combination of the two results in the overall smallest uncertainty by assigning a weight to the two measurement and model. To make this possible, the variance of both the measurement noise and process noise needs to be known. Since this is not the case during this work, a method to calculate this is introduced: unscented transform. This looks similar to the well-known Monte-Carlo simulation, except that a deterministic set of inputs is used that results in the smallest possible amount of computations to calculate the result. These two algorithms can be combined in a unscented Kalman filter, which has the some advantages over a regular Kalman filter: the process can be non-linear and the standard deviation of the noise doesn't need to be known as an input.

A much used method to compute the state of the system in presence of noise is using a Kalman filter [25]. This recursive algorithm has the advantage that it can be run in real-time, updating its estimate after every time-step. Computing the states however does require knowledge of the noise and the linear ordinary differential equations (ODE) that describe the process. Since this is not the case during this work an extension of the Kalman filter, called the unscented Kalman filter [21], is used. Using this filter no knowledge of the noise is needed and the system can be non-linear. This section starts out explaining how a regular Kalman filter works, and discusses the unscented transform [20] next. This method looks similar to a Monte-Carlo simulation and can be used to calculate the uncertainty or covariance of an unknown process. It will be combined with the Kalman filter to derive the filter of choice: an unscented Kalman filter.

2.3.1 Linear Kalman filter

The state space equation for a linear time-invariant is given by:

$$x_k = Fx_{k-1} + Gu_{k-1} + w_{k-1} \tag{2.11a}$$

$$y_k = H_k x_k + v_k \tag{2.11b}$$

In this equation, the state x_k depends on the previous state, x_{k-1} multiplied with the system matrix in the previous state F while the input of the previous state, u_{k-1} gets multiplied with the input matrix G. This gets added to the term with the system matrix including the process noise w. The output of the system, y_k, can be obtained by taking the current state and multiply it with the output matrix H_x and adding the term for measurement noise v_k.

For the noise terms we assume that they are strictly white-noise and that w_k has the covariance matrix Q_k and v_k has covariance matrix R_k. These matrices cause the process to be stochastic instead of deterministic that is common for observers.

The Kalman filter algorithm is made up out of two parts, a prediction part and an update part. As a result we need to introduce an additional notation, one for the 'a priori' and one for the 'a posteriori' state. The estimated a posteriori state is denoted by $\hat{x}$ while the estimated a prior state is denoted by $\hat{x}^-$ where the minus sign refers to the priori state.

Using this notation, the Kalman filter equation are:

$$\hat{x}_k^- = F\hat{x}_{k-1} + Gu_{k-1} \tag{2.12a}$$

$$P_k^- = FP_{k-1}F^T + Q \tag{2.12b}$$

$$K_k = P_k^- H^T (HP_k^- H^T + R)^{-1} \tag{2.13a}$$

$$\hat{x}_k = \hat{x}_k^- + K_k(y_k - Hx_k^-) \tag{2.13b}$$

$$P_k = (I - K_kH)P_k^-(I - K_kH)^T + K_kR_kK_k^T \tag{2.13c}$$

Two new terms have been introduced. The first is P_k, which is the error covariance of the estimated state. At P_0 this is the error covariance in the initial state x_0 and $\hat{x}_0$.

The second term is K_k, which is the Kalman gain. The Kalman gain shows how accurate the a posterior is compared to the a priori state. When K is small the measurement noise, R, is large and covariance error of the a priori state, P_k^-, is small. As a result more weight should be given to the model than the measurement.

2.3.2 Unscented transform

This subsection provides the background needed to understand the unscented transform. Proposed by Julier et.al [20], the idea of the unscented transform is that it is easier to calculate the resulting mean and variance of a non-linear process than it is to determine the non-linear function. A process which resembles a Monte-Carlo simulation is used, but instead of feeding random perturbed data to the non-linear system and reconstructing the mean and variance from the output, a clever set of data points is picked. It will be shown that this greatly reduces the amount of calculations needed to calculate the final result and that the result is exact for the mean and variance while the skewness can be approximated very well.

Algorithm

Suppose there is a nonlinear function f with an input vector x and an output y. The nonlinear function is unknown, as are the mean of y, denoted with $\bar{y}$ and the covariance matrix of y, P_{yy}. From the input the mean and the covariance is known, $\bar{x}$ and P_{xx}.

We now state that it is possible to determine $\bar{y}$ and P_{yy} if we pick an amount of data points, called σ-point, and propagate these through the nonlinear function. The results can be used to reconstruct the mean and covariance exact and higher order terms can be approximated accurately. Proof for this can be found in work by Julier et al [20].

The σ-points should be chosen as follows:

$$\chi_o = \bar{x}, \tag{2.14a}$$

$$\chi_i = \bar{x} + \sqrt{(L+\lambda)P_{xx}}_i, \quad i = 1, ..., L, \tag{2.14b}$$

$$\chi_i = \bar{x} - \sqrt{(L+\lambda)P_{xx}}_i, \quad i = L+1, ..., 2L \tag{2.14c}$$

In these equations, L is the dimension of x and λ is a scaling parameter. This scaling parameter is defined as:

$$\lambda = \alpha^2(L + \kappa) - L \tag{2.15}$$

A scaling parameter is introduced, κ. This parameter is only important for the higher order statistical terms such as the skewness. A rule of thumb is to set it in such a way that $\kappa = 3 - L$. Parameter α is used to determine the spread of the σ-points around $\bar{x}$, and is picked between a small, positive number and 1. Increasing α is usually done to remove the effect of higher order terms.

The σ-points can now be propagated through the nonlinear function:

$$\mathcal{Y}_i = f(\chi_i), \quad i = 0, ..., 2L \tag{2.16}$$

It is now possible to determine $\bar{y}$ and P_{yy}:

$$\bar{y} = \sum_{i=1}^{2L} \frac{1}{2(L+\lambda)} \mathcal{Y}_i + \frac{\lambda}{L+\lambda} \mathcal{Y}_0 \tag{2.17a}$$

$$P_{yy} = \sum_{i=1}^{2L} \frac{1}{2(L+\lambda)} (\mathcal{Y}_i - \bar{y})(\mathcal{Y}_i - \bar{y})^T + (\frac{\lambda}{L+\lambda} + 3 - \alpha)(\mathcal{Y}_0 - \bar{y})(\mathcal{Y}_0 - \bar{y})^T \tag{2.17b}$$

A scheme about the algorithm is shown in figure 2.2. Here is single example is used with $L = 1$.

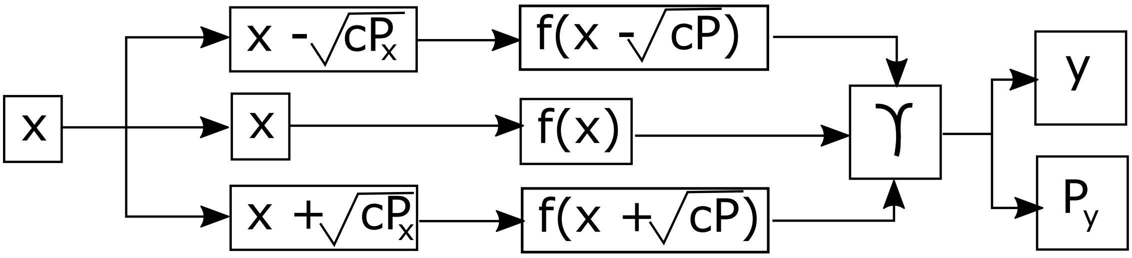

Figure 2.2: Simple example of an unscented transform. The single value for x gets expanded with the square root of the standard deviation and a correction term. These values get put through the nonlinear function F and combined in $\mathcal{Y}$. From here y and the variance of y can be determined.

A few things should be noted about this result. First of all, the newly introduced terms that are a function of λ and L can be negative. Summing these terms together for each of the equations results in 1, and as a result they should be thought of as scaling as a function of the amount of dimensions. Not doing this results in drifting away from σ - points around $\bar{x}$, causing the mean and variance to be dependent on the amount of sample points. Second result is that finding the mean and variance did not require any matrix inversion or knowledge about the nonlinear function. This results in a computational cheap result. The same calculation can be made using a Monte-Carlo simulation, however unscented transform requires the perturbation of $2L + 1$ data points while Monte-Carlo requires order of magnitude more.

2.3.3 Unscented Kalman filter

Now that unscented transform and a 'regular' Kalman filter have been introduced, it is possible to combine it to construct an Unscented Kalman filter [21]. The advantage of such a filter is that it is possible to apply it if the process is described by non-linear ODE's. It is also more accurate than similar filters such as the Extended Kalman filter. At the end of that subsection it has also been pointed out that during unscented transform, there is no need to take the inverse of a matrix. This has the advantage of speeding up the process significant, especially for large systems.

A schematic overview of the algorithm can be found in figure 2.3 and the algorithm has been described afterwards.

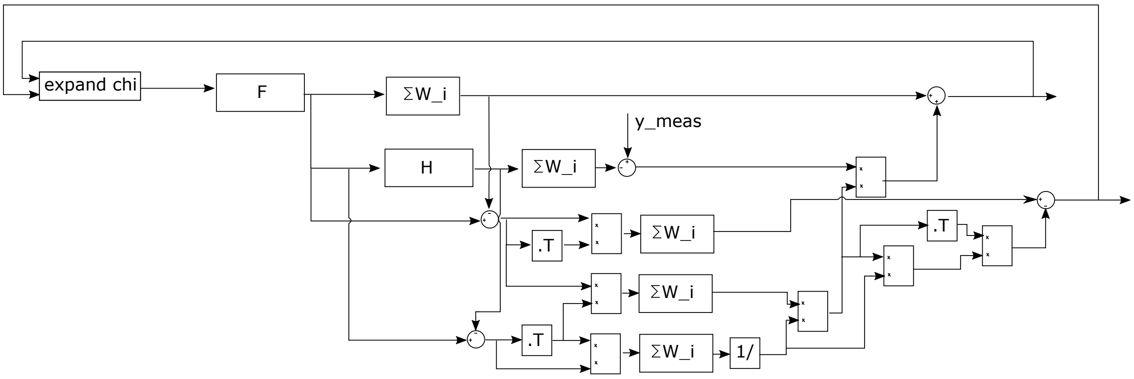

Figure 2.3: Block scheme of the unscented Kalman filter. Nonlinear functions F and H can be seen, as well as the operation to generate the χ-vector and the summations using the weights to calculate, for example, P. The only input is the measurement data y_{meas}.

Initialize:

$$\hat{\boldsymbol{x}}_0 = \mathbb{E}[\boldsymbol{x}_0] \tag{2.18}$$

$$\boldsymbol{P}_0 = \mathbb{E}[(\boldsymbol{x}_0 - \hat{\boldsymbol{x}}_0)(\boldsymbol{x}_0 - \hat{\boldsymbol{x}}_0)^T] \tag{2.19}$$

Calculate σ-points:

$$\boldsymbol{\chi}^a_{k-1} = [\hat{\boldsymbol{x}}^a_{k-1} \quad \hat{\boldsymbol{x}}^a_{k-1} + \gamma\sqrt{\boldsymbol{P}^a_{k-1}} \quad \hat{\boldsymbol{x}}^a_{k-1} - \gamma\sqrt{\boldsymbol{P}^a_{k-1}}] \tag{2.20}$$

Time-update equations:

$$\boldsymbol{\chi}^{\chi}_{k|k-1} = \boldsymbol{F}\big(\boldsymbol{\chi}^{\chi}_{k-1}, \boldsymbol{u}_{k-1}, \boldsymbol{\chi}^{v}_{k-1}\big) \tag{2.21}$$

$$\hat{\boldsymbol{x}}^-_k = \sum_{i=0}^{2L} W^{(m)}_i \chi^{\chi}_{i,k|k-1} \tag{2.22}$$

$$\hat{\boldsymbol{P}}^-_k = \sum_{i=0}^{2L} W^{(c)}_i \big(\chi^{\chi}_{i,k|k-1} - \hat{\boldsymbol{x}}^-_k\big)\big(\chi^{\chi}_{i,k|k-1} - \hat{\boldsymbol{x}}^-_k\big)^T \tag{2.23}$$

$$\boldsymbol{\mathcal{Y}}_{k|k-1} = \boldsymbol{H}\big(\boldsymbol{\chi}^{\chi}_{k|k-1}, \boldsymbol{\chi}^{n}_{k-1}\big) \tag{2.24}$$

$$\hat{\boldsymbol{y}}^-_k = \sum_{i=0}^{2L} W^{(m)}_i \mathcal{Y}_{i,k|k-1} \tag{2.25}$$

Measurement-update equations:

$$\boldsymbol{P}_{\boldsymbol{y_k y_k}} = \sum_{i=0}^{2L} W^{(c)}_i \big(\mathcal{Y}_{i,k|k-1} - \hat{\boldsymbol{y}}^-_k\big)\big(\mathcal{Y}_{i,k|k-1} - \hat{\boldsymbol{y}}^-_k\big)^T \tag{2.26}$$

$$\boldsymbol{P}_{\boldsymbol{x_k y_k}} = \sum_{i=0}^{2L} W^{(c)}_i \big(\chi_{i,k|k-1} - \hat{\boldsymbol{x}}^-_k\big)\big(\mathcal{Y}_{i,k|k-1} - \hat{\boldsymbol{y}}^-_k\big)^T \tag{2.27}$$

$$\mathcal{K}_k = \boldsymbol{P}_{\boldsymbol{x_k y_k}} {\boldsymbol{P}_{\boldsymbol{y_k y_k}}}^{-1} \tag{2.28}$$

$$\hat{\boldsymbol{x}}_k = \hat{\boldsymbol{x}}^-_k + \mathcal{K}_k(\boldsymbol{y}_k - \hat{\boldsymbol{y}}^-_k) \tag{2.29}$$

$$\boldsymbol{P}_k = \boldsymbol{P}^-_k - \mathcal{K}_k \boldsymbol{P}_{\boldsymbol{y_k y_k}} \mathcal{K}^T_k \tag{2.30}$$

Comparing this algorithm with the unscented transform algorithm and the Kalman filter algorithm, the similarities are easily seen. One new variable is introduced, $\gamma = \sqrt{L + \lambda}$. The only data that is needed to execute this algorithm are the non-linear functions $\boldsymbol{F}$ and $\boldsymbol{H}$, states x and the covariance matrix P. From this, the σ-points can be constructed. These can be fed through the non-linear equations, making it possible to reconstruct properties such as the covariance of the output and Kalman filter properties such as the Kalman gain.

Chapter 3

Experiment and Code

The data that is being used is from the nuclear fusion reactor 'DIII-D' at General Atomics. The reactor is briefly introduced as a well as important diagnostics for this work. A theoretical background will be provided to get a sense of how the data is gathered and which properties can be measured.

Processing the data in usable data is done using two codes: the Consistent Automatic Kinetic Equilibrium (CAKE) code and DCON. This chapter will give an overview of how CAKE works and how the kinetic constraints are formed and how these are processed into an equilibrium using EFIT. After that, it will be explained how it can be seen if the profiles constructed by CAKE can be considered good by studying the χ^2 and Grad-Shafranov errors.

After it has been established that kinetic profiles can be produced in large quantities of sufficient quality, the next step will be introduced: DCON. This code uses a novel way of finding the least stable mode by studying the plasma response matrix.

The chapter concludes with a section about the effects of the various diagnostics that CAKE uses on the output of DCON. Knowing which diagnostics have a large impact on the final result helps determining the minimum amount of required diagnostics before the results from DCON can be trusted.

3.1 DIII-D and diagnostics

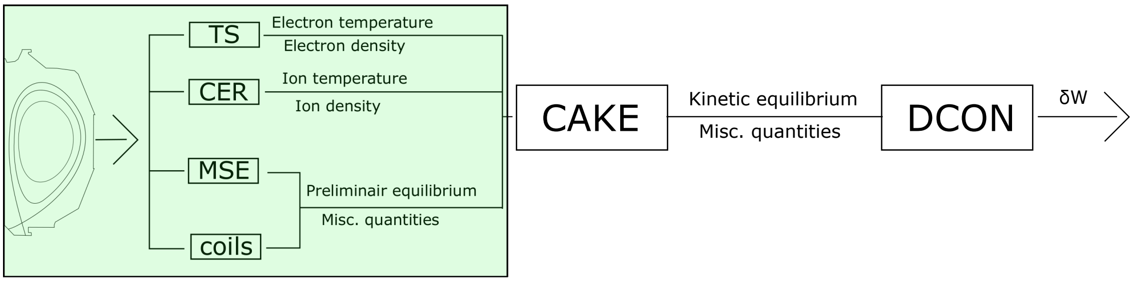

Figure 3.1: Overview of the experiment, diagnostics and codes used to calculate δW. Data moves from left, DIII-D reactor, to the right by 4 types of diagnostics and the CAKE / DCON codes.The green shaded area shows the part that is being discussed in this section.

One of the largest operating shaped tokamaks is located at General Atomics in San Diego, USA. The tokamak is called DIII-D [26], being named after the D-shaped plasma. DIII-D is an upgrade of the Doublet III reactor, when it became clear that a D-shaped plasma has advantages such has high β and suppression of certain groups of instabilities resulting in a high performance plasma. Being in operation since 1978 and being further developed in the 1980s, it achieved several milestones such as highest plasma β at that time and it played a leading roll in the application of Neutral Beam Injection (NBI) to heat the plasma. In recent years, the focus has been on running advanced plasma scenarios such as the 'ITER baseline scenario' to mimic the expected shape of ITER and the 'Quiescent H-mode', an improved H-mode without sawteething and improved confinement.

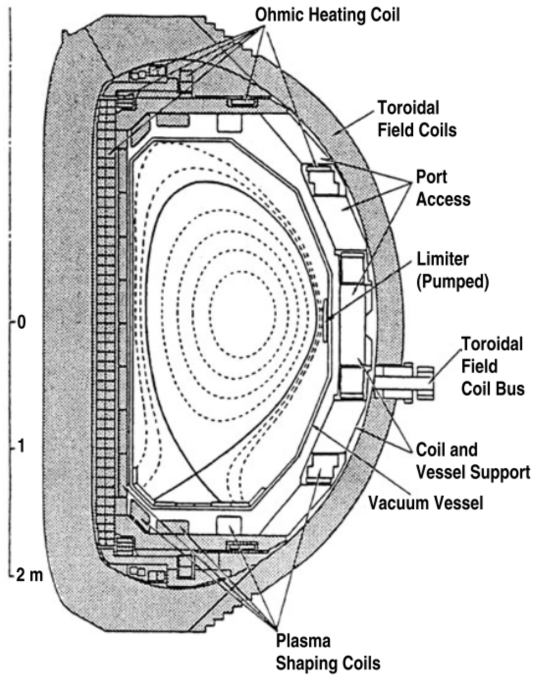

Figure 3.2: Cross-section of the DIII-D tokamak. Locations of the coils are shown, as well as locations of diagnostic points. Original from work by Luxon et al.[27]

Figure 3.2 shows a cross-section of DIII-D. The location of various coils are depicted, as well as the vacuum vessel and a limiter. Inside the vessel, an example of a plasma scenario is depicted, with magnetic field lines depicted in dashed lines. The last closed flux surface is depicted in a solid black line, and an x-point can be seen in the bottom of the machine. It should be noted that DIII-D has the capability to also run plasma where the x-point is in the top of the vessel or with two x-points. Data used in this thesis is from the DIII-D reactor, using the x-point in the bottom configuration.

3.1.1 DIII-D diagnostic used by CAKE

The reconstruction of the plasma equilibrium at DIII-D is currently done by using magnetics data and using Motional Stark Effect (MSE) diagnostics. This combination makes it possible to get a rough pressure profile (using magnetics) and a fairly good current density profile (MSE). However, the pressure profile is missing various important physical features such as the pedestal. To improve the equilibrium in the pedestal region, data about the local pressures can be gathered from the Thomson Scattering (TS) and Charge Exchange Recombination (CER) diagnostics and used to constrain the Grad-Shafranov solver.

This section gives a brief introduction to the three most important diagnostics for this work: CER, TS and MSE. While other diagnostic tools have been used for the equilibrium reconstruction, such as magnetics, the inclusion of these have had the biggest effect on the results from CAKE.

Thomson scattering at DIII-D

Thomson scattering (TS) [28, 29, 30] is the diagnostic of choice to determine properties of the electrons in a fusion plasma. TS is the process of the scattering of electromagnetic waves by free electrons. The scattering of the monochromatic electromagnetic radiation is caused due to the Doppler effect. Looking at the scattering, it is possible to locally determine the electron density (n_e) and temperature (T_e). The measurement locations are depicted in figure 3.3 with blue and red squares. It can be seen that especially in the outer regions of the plasma a high spatial resolution is available. The pedestal region is viewed by 20 chords with a spacing of $6mm$ and a scattering length of $5mm$ sampled at a nominal rate of 250Hz, making it possible to accurately determine electron properties in the plasma edge.

Charge exchange recombination at DIII-D

Charge Exchange Recombination spectroscopy (CER) [32, 33] is used to determine properties of the ions in the fusion plasma. CER studies the emission caused by the interaction between neutral particles and the hot plasma. It is possible to determine the ion temperature (T_i), density (n_i) and the plasma rotation velocity as well as impurity concentrations, but the first two are most important for this work.

CER only works in combination with neutral beam injection (NBI) [3]. When the neutral particles get fired in to the plasma, with the purpose of heating and fueling the plasma, an intense charge exchange recombination reaction appears at the location of the beam. A sketch of the setup can be seen in figure 3.4. It can be seen that there is a higher spatial resolution in the edge, making it possible to accurately measure the pedestal. CER is studied both co- and counter the plasma current.

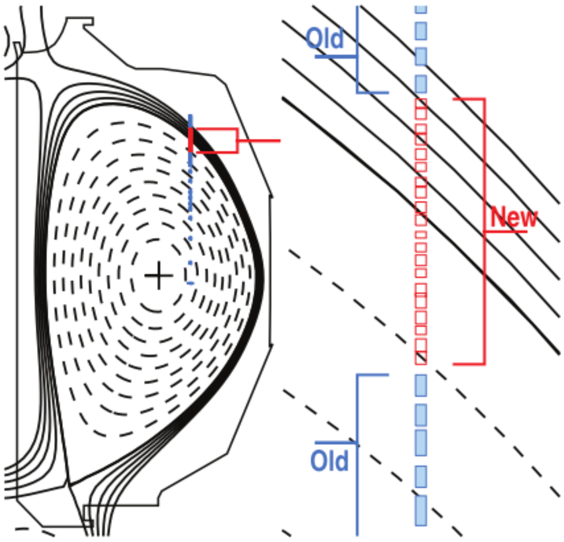

Figure 3.3: Upgraded Thomson scattering (TS) diagnostics of DIII-D. Blue depicts the original location of the lasers while red depicts the new locations. Original from D. Eldon et al.[31]

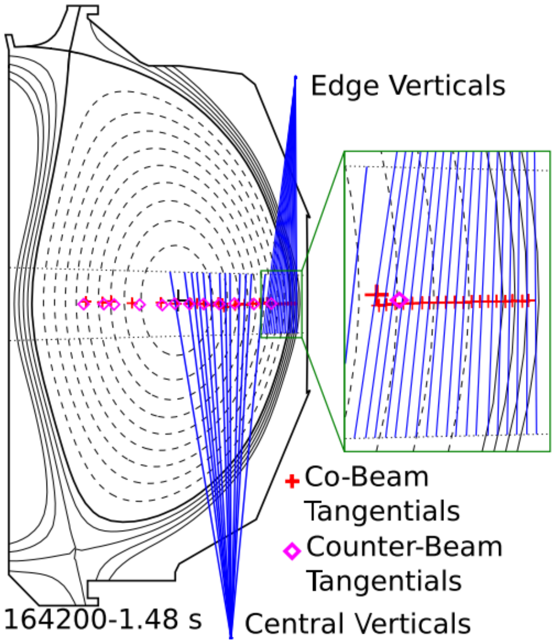

Figure 3.4: Upgraded Charge Exchange Recombination (CER) diagnostics of DIII-D. The co and counter tangential beams are depicted in red and purple respectively. Vertical channels are depicted in blue, but are not used in this work for the equilibrium construction. Original from [32]

Motional Stark effect at DIII-D

The Motional Stark Effect (MSE) [34, 35] is a diagnostic that can be used to aid in the reconstruction of kinetic profiles. Like CER, it is dependent on the presence of fast ions due to NBI, but it can measure the pitch angle, which is defined as:

$$\gamma_{pitch}(r) = arctan(\boldsymbol{B_\theta}(r)/\boldsymbol{B_\phi}) \tag{3.1}$$

Using this, it is possible to express the $q(r)$ as a function of the pitch angle:

$$q(r) = \frac{r}{R\gamma_{pitch}(r)} \tag{3.2}$$

Experiments have shown that MSE is an accurate way of predicting the q-profile of a plasma and as a result the magnetic topology. It is especially effective in the hot regions of the plasma near the core.

DIII-D has five operational MSE polarimeters[35]. These view a NBI that is injected counter to the plasma current since experiments at DIII-D have shown that this is a more favorable setup than the radial MSE core view.

3.2 Consistent Automatic Kinetic Equilibrium (CAKE)

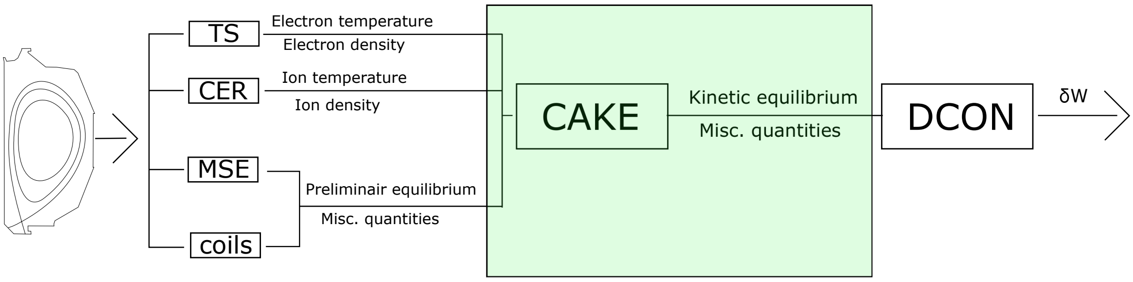

Figure 3.5: Overview of the experiment, diagnostics and codes used to calculate δW. Data moves from left, DIII-D reactor, to the right by 4 types of diagnostics and the CAKE / DCON codes.The green shaded area shows the part that is being discussed in this section.

Solving the Grad-Shafranov equation is done at DIII-D [26] using the EFIT code[18]. When given a set of constraints as inputs it solves the Grad-Shafranov equation as a minimization problem using a cost function resulting in the pressure and current density profiles as outputs. Original EFIT only uses data from magnetics and is used for a few decades now. More recently, the quality of equilibria further improved by using MSE-data[35]. This solution however still misses important physical properties. For this purpose the Consistent Automatic Kinetic Equilibrium (CAKE) code is developed at Princeton University, General Atomics and Eindhoven University of Technology [19]. This code is the subject of this section, starting with a description on how to EFIT works, explaining how the so-called 'kinetic constraints' are applied and ending with an explanation on how to verify the accuracy of the results.

3.2.1 EFIT

The EFIT code is a way of evaluating the Grad-Shafranov equation based on measurements and other constraints given as input. Recall the Grad-Shafranov equation:

$$\Delta^\star \psi = -\mu_0 R^2 P' - FF' \tag{3.3}$$

The free functions P' and FF' can be formulated as polynomials that depend on the linear coefficients α_n and β_n:

$$P'(\psi) = \sum_{n=0}^{n_P} \alpha_n x^n - x^{n_p+1} \sum_{n=0}^{n_P} \alpha_n \tag{3.4a}$$

$$FF'(\psi) = \sum_{n=0}^{n_F} \beta_n x^n - x^{n_p+1} \sum_{n=0}^{n_F} \beta_n \tag{3.4b}$$

In these equations x is the ratio $(\psi - \psi_m)/(\psi_b - \psi_m)$ where ψ_m is the poloidal flux at the magnetic axis and ψ_b is the poloidal flux at the boundary. It is assumed at P' and FF' are equal to zero at the boundary. The total amount of coefficients $(n_P + n_F + 2)$ depends on the available measurements and the total number of imposed constraints and is determined empirically.

To solve for α_n and β_n, a χ^2-error is minimized:

$$GSerror = \sum_{i=1}^{n_M} \left(\frac{M_i - C_i}{\sigma_i} \right)^2 + \sum_{i=1}^{n_C} \left(\frac{H_i - D_i}{\eta_i} \right)^2 \tag{3.5}$$

The GSerror consists of two terms: a measurement term and a constraint term. The measurement term is made up out of the i-th measurement value, M_i, the i-th computed value C_i and the corresponding uncertainty σ_i. Examples of quantities that are calculated in this term are the poloidal fluxes, the poloidal magnetic field and the total current. The calculation of these variables for C_i is done by reformulating the Grad-Shafranov equation using integrals by applying a toroidal Green's function and using a Picard iteration scheme to obtain the solution:

$$C_i^{(m+1)}(\overline{r}_i) = \sum_{n=1}^{n_e} G_{C_i}(\overline{r}_i, \overline{r}_{en}) I_{en}^{m+1} + \int_{\Omega_m} dR' dZ' G_{C_i}(\overline{r}_i, \overline{r}') j_\phi(R', \psi^m, \alpha_n^{m+1}, \beta_n^{m+1}) \tag{3.6}$$

In this equation, m is the iteration number, n_e is the number of external shaping coils, I_{en} the current in the coil located at location $\overline{r}_{en}$ and Ω_m is the plasma volume. The toroidal current density is denoted by j_ϕ.

The second part of the GSerror is for additional applied constrains that are not calculated using equation 3.6. It has the same structure as the measurement term: H_i being the i-th imposed constraint, D_i the calculated result and η_i being the uncertainty of the calculation.

Constraints will be added by CAKE resulting in a 'kinetic profile'. Thomson scattering and CER are being used to calculate the density and temperature profiles of electrons and ions. This can be used to determine additional pressure constraints by $P = P_e + P_i + P_z + P_{fast} = n_e T_e + n_i T_i + P_z + P_{fast}$. The fast ion pressure, P_{fast} is determined by using a code called ONETWO, more on that in the next section.

The current profile also gets additional constraints. It is possible to use Sauter's equation to get an estimate for the bootstrap current. The bootstrap current is due trapped particles and passing particles interacting with each other, and is dominant in near the edge of the plasma. As a result, CAKE only adds current density constraints towards the edge of the plasma but not in the core.

3.2.2 Kinetic constraints

In figure 3.6 an overview of the workflow from CAKE has been given. This section will describe the steps more in detail. The code can be separated in 4 sections: gathering, fitting, constraint forming and running EFIT.

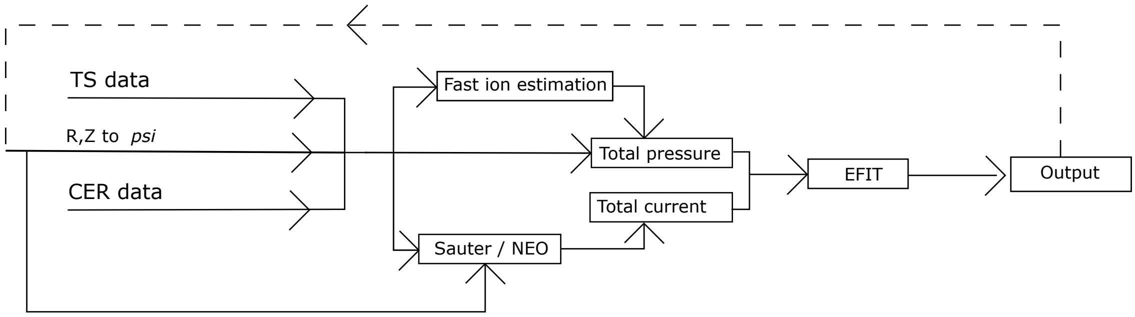

Figure 3.6: The workflow of the CAKE code. TS data, R,Z to ψ_n and CER data is collected and moves from left to right in the figure until output is reached. If an iteration, to map diagnostic data using CAKE is preferred, the output is returned (dashed line) and the process starts over.

Gathering

The process starts by gathering data from various diagnostics from the DIII-D database. The software which runs this database is called 'MDSplus' and as a result the database is often referred to as 'MDSplus', as will be in this work. The data can be categorized in four types: CER data, TS data, a g-file and supporting data.

The g-file is the output from EFIT and contains information about the plasma equilibrium. Output from a version of EFIT is always present, the quality can however be poor. They however serve as excellent starting points for the mapping for TS and CER data from R, Z-coordinates to the required $\psi_n(R, Z)$ coordinates. Using this method is very fast, it however introduces a small error since the g-file used for mapping is different from the g-file produced by CAKE.

TS and CER data is being filtered for outliers and unphysical values. Data is scanned for outliers by studying the fractional uncertainties for different ranges. To make the code more robust for these mistakes, a minimum error is enforced on all data points.

Fitting

After the TS and CER has been cleaned and mapped to the ψ_n-grid, it is possible to fit the properties that are needed for the work flow. CER data is used to determine the ion density and temperature profile while TS data is used to determine the electron density and temperature.

An example of fitted data can be seen in figure 3.7. It displays the 4 main fitted results, the last closed flux surface is depicted as a dashed line. The red data points are the filtered data from the previous step. The blue line depicts the fitted data while the shaded area represents the uncertainty. The types of fits that have been used are included in the caption in the figure. Two types of fitting methods are used: tanh-fit based and Monte-Carlo based. Monte-Carlo splines are cast thousands of times with different knotting locations. The best result, the one that has the smallest residual error, is then used. For the tanh-fits a $tanh(x)$ function is used to fit the pedestal area while a polynomial is used to fit the core. Testing shows that properties that show a steep pedestal, which are the densities and the electron temperature can best be fit using tanh. The ion temperature shows best results using a Monte-Carlo spline. One very important effect from using Monte-Carlo fitting is that noise is introduced in the calculation.

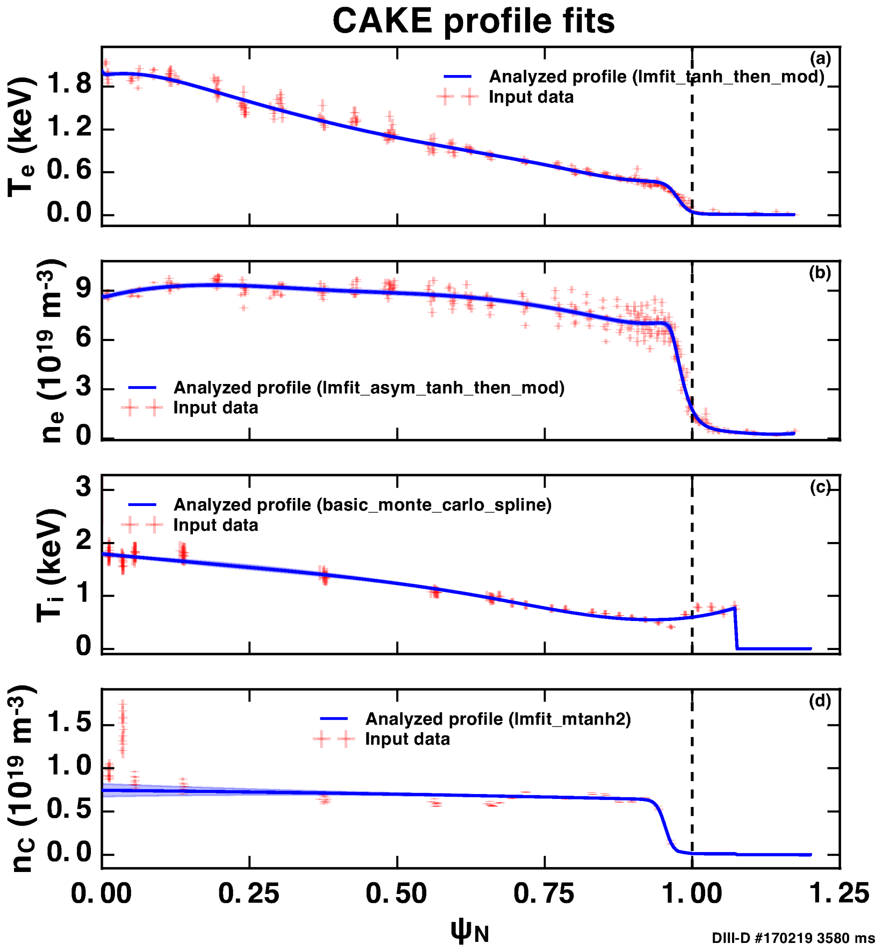

Figure 3.7: Example of fitting data for shot 170219 at 3580ms. Red crosses denote the cleaned data and the blue line is the fit that was deemed best. De dashed line at $\psi_n = 1$ denotes the last closed flux surface. The fitting method that has been used is noted in the legend.

Constraint forming

After the profiles have been fit, so T_i,n_i,T_e and n_e are known and a first estimate for the magnetic topology has been collected from the g-file, it is possible to calculate the last two parts of the constraints: bootstrap current profile and the fast ion pressure. For the fast ion calculation two options are available: assuming a fraction of the electrons or using a code called ONETWO [36]. This transport code is used at General Atomics and predicts the effect of fast ions by using a model by Callen [36] for the slowing down of fast ions and empirically determined fast ion profiles in DIII-D.

An example of the pressure constraint and its sub-constraints, including the uncertainties, can be seen in figure 3.8.

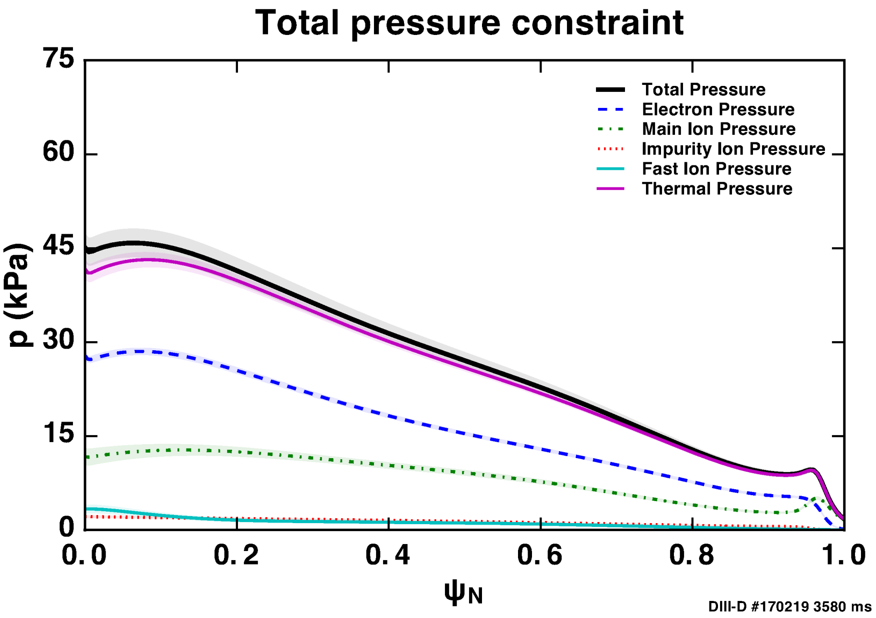

Figure 3.8: Pressure constraints calculated by CAKE. In black the total current constraint can be seen. The thermal pressure is the total pressure without the impurity ion pressure calculated by ONETWO using CER data. The electron and ion pressure are calculated using data from Thomson scattering and CER respectively. The fast ion pressure is calculated by ONETWO using both CER and Thomson scattering.

Constraints for the current density are more complex, with the total current density given by: $J = J_{Bootstrap} + J_{Ohmic} + J_{NBCD} + J_{ECCD}$. The bootstrap current can be calculated using Sauter's equation [37, 38].

A byproduct of applying Sauter's equation is that it is also possible to get neoclassical conductivity, σ_{NC}. If it is assumed that there is no spatial variation in the loop voltage and that the current profile is relaxed, the Ohmic current is proportional to the neoclassical conductivity. Since I_p can be determined accurately, it is possible to subtract the bootstrap current and scale J_{Ohmic} until the total I_p matches the experiment.

If there is data present from MSE, this is used to calculate the current density profile in the core instead of using the Ohmic current density. This is because MSE is accurate in the core and during the calculation of the Ohmic current multiple assumptions where made. In the edge, however, the bootstrap current is the dominant factor so the results from Sauter's equation are used instead. This is because here the situation is reversed: Sauter's equation is fairly accurate but the MSE diagnostic results aren't [37, 38].

Calculating the contribution due to NBCD and ECCD is not implemented in CAKE yet. It is not expected that the lack of this data has a significant impact on the current density profile since most constraints used as an input for EFIT of the current density profile are located in the edge region where the contribution of NBCD and ECCD is minimal. Figure 3.9 shows the current density constraints that are being used as an input for EFIT.

Run EFIT

After the constraints have been generated, it is possible to run EFIT. Execution time linearly increases with the amount of time slices, as can be seen in figure 3.10. This setup is using the most time consuming processes, which are running EFIT, running ONETWO and collecting data

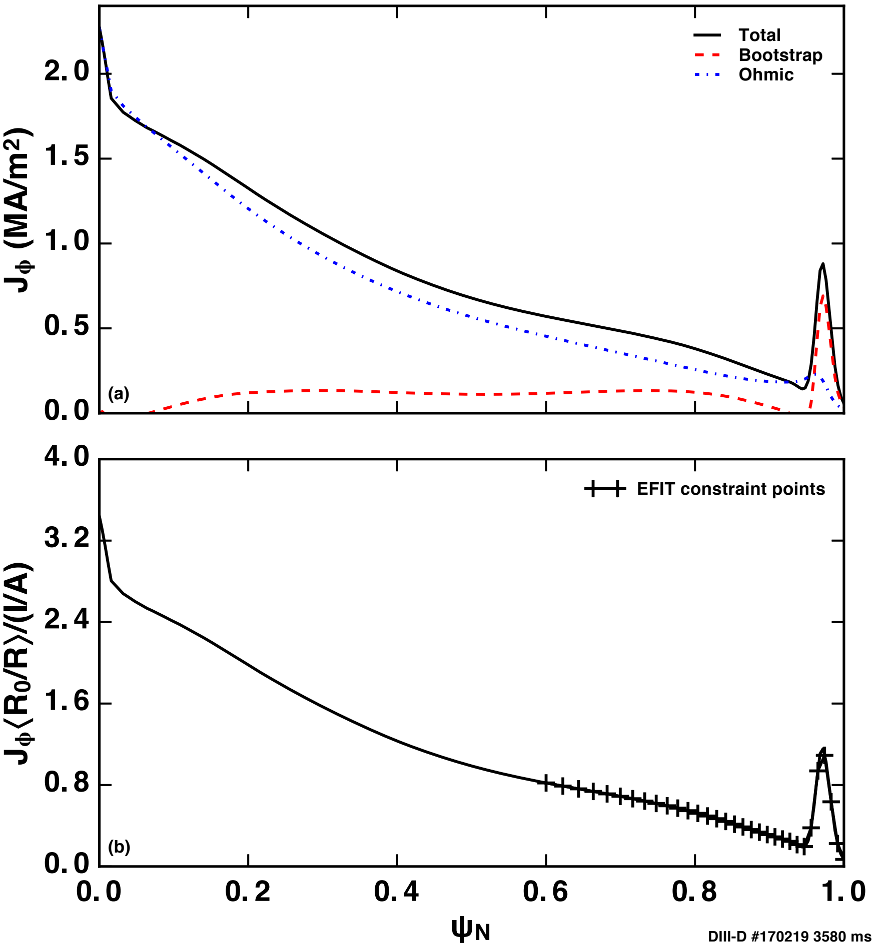

Figure 3.9: Current constraints calculated by CAKE. The bootstrap current density is calculated using Sauter's equation.The Ohmic current density is estimated by subtracting the bootstrap current density from the total estimated current density. In the bottom figure, the black crosses show the constraints used for EFIT. For the core Motional Stark effect data is used if it is available. If this is not the case, no current density constraints are given to EFIT for the core due to a large inaccuracy.

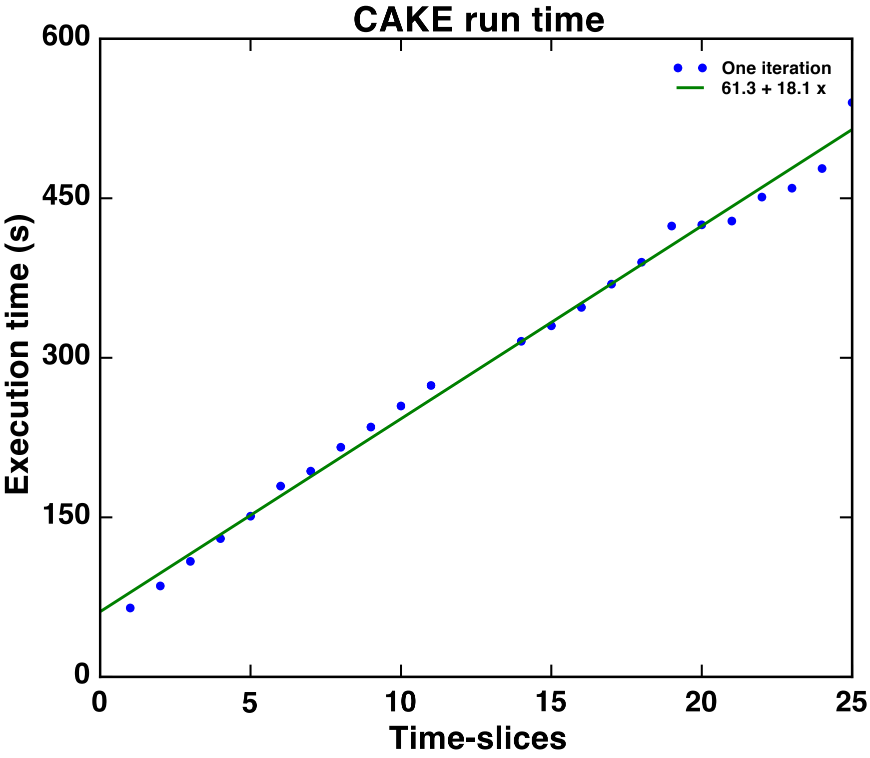

Figure 3.10: CAKE execution time for a single iteration.

from the MDSplus-tree. It can be seen that the execution time is roughly $60s$ with an overhead of about $18s$. Adding a second iteration, meaning running CAKE again only using the output from the original CAKE run for the mapping of the TS and CER data, yields a total computation time of $80s$ per time slice. The increase in speed is attributed to the fact that all the data that needs to be collected is already stored locally.

3.2.3 Verifying the results

After the above procedure has been followed, the plasma equilibrium has been reconstructed with additional kinetic constraints. An example of such a profile can be seen in figure 3.11, where in the top figure the pressure is plotted and in the bottom figure the current density profile and the original, non kinetic results, are plotted as a dashed line.

A first visual inspection shows that this is indeed what we are looking for. In the edge region, the pedestal can clearly be seen as well as a peak due to the bootstrap current. Going towards the core, both functions are continuous and either constant or increasing.

Results from the equilibrium reconstruction are difficult to verify using experimental data since there is no additional independent data that we can compare the results with. However, two properties can be studied: the Grad-Shafranov error and the χ^2 error.

The Grad-Shafranov error is defined as equation 3.5. Typical results for EFIT01 are in the order of 10^{-4} but when edge calculations are done or stability analysis is performed with different codes an error in the order of 10^{-8} is preferred. If the error is unusually big this could mean that there is a mismatch between the constraints used as input and the solution to the Grad-Shafranov equation. A situation in which this may occur is when there is a large island present in the plasma. In this

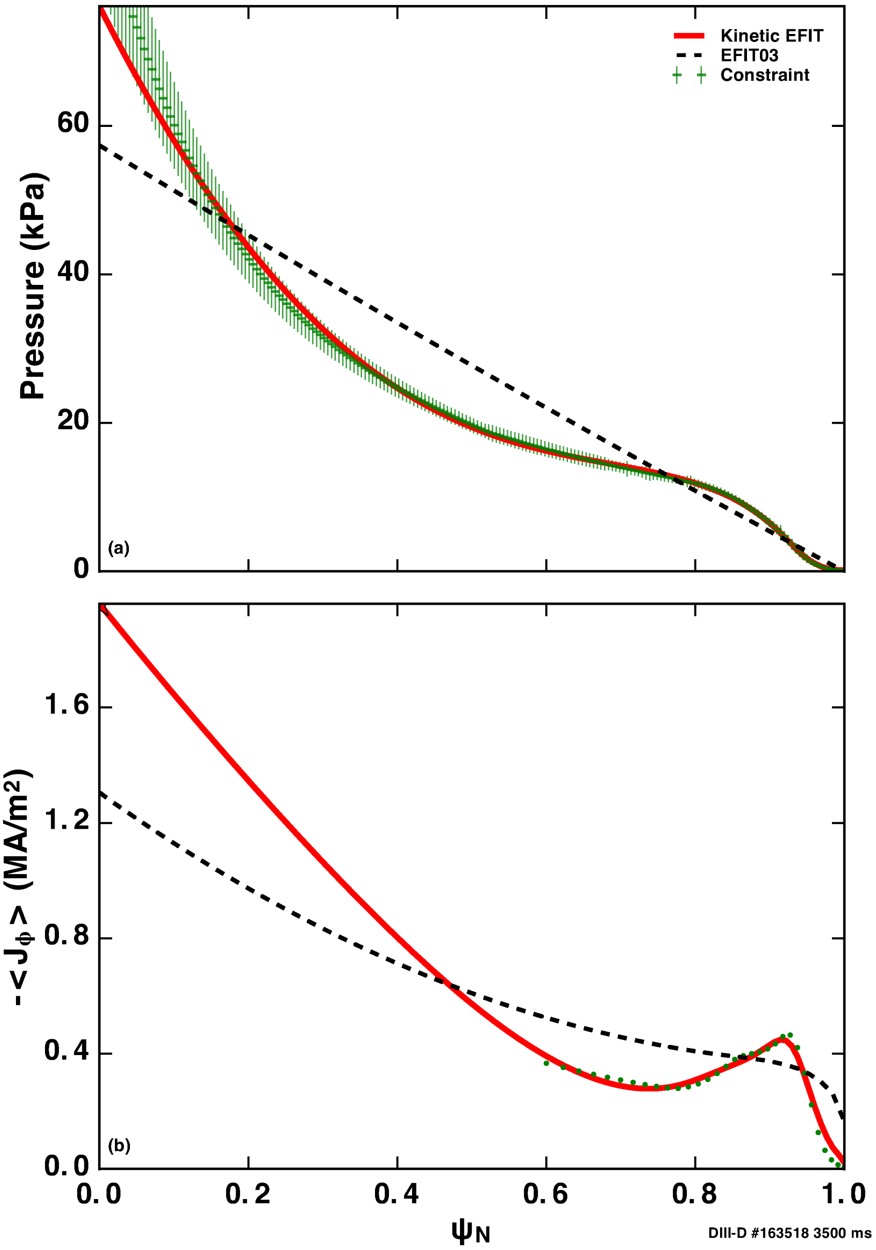

Figure 3.11: Final result from CAKE.Top: pressure profile as a function of ψ_n. Bottom: current density profile as a function of ψ_n. The pedestal can be clearly seen at the edge of the plasma. A final visual inspection can be done by making sure the values are all positive and having continuous functions. The pressure at $\psi_n = 1$ should be equal to 0, while the current density should be 'sufficiently small'.

case the Grad-Shafranov equation does not hold and the error would be large. A more subtle cause might be due to the presence of an ELM in the averaging window. If the diagnostics data before and after an ELM are averaged, the resulting profiles would be a strange combination that can not converge well using the Grad-Shafranov equation.

For the rest of this thesis CAKE is configured in such a way that it tries to converge to an error of 10^{-8} or it stops after 150 iterations. Resulting CAKE profiles that have an Grad-Shafranov error of 10^{-8} or smaller are considered 'good'. Profiles that are between 10^{-4} and 10^{-8} are considered sufficient while profiles that are bigger should be inspected.

Now that we have determined how well the calculated constraints match the Grad-Shafranov equation, it is also important to study how close the unfitted diagnostic data matches the final profiles. If for example the resulting pressure and current density profile differ a lot from measurement data but has a low Grad-Shafranov error, results are still considered bad. Determining how close the results are from diagnostics to the final results can be done by determining the χ^2 through:

$$\chi^2 = \sum \frac{(Diag_i - Eq_i)^2}{\sigma_i^2} \tag{3.7}$$

This equation is the same as the Grad-Shafranov error, however this time it looks at the error between the input diagnostic compared to the output profile. The Grad-Shafranov error compares the constraints (processed diagnostic data) to the output profile.

The result is an output from CAKE, and it is calculated for 4 properties: flux loops, magnetic probes, MSE and the pressure. If one of these values is unexpectedly high the resulting profiles should be studied. It would mean that the resulting profile would not match the diagnostic data. This happens if there is a lack of good data, causing bad fits early on in the process.

An example figure on the output quality is given in figure 3.12. Discharge 163518 has been sampled 11 times during the time interval between 3200ms and 4200ms, once every 100ms with an averaging window of 50ms. In the top figure, the χ^2 has been plotted. The first thing that should be noticed is that there was no MSE data present during these times, resulting in a χ^2 of 0 for all data points. If χ^2 is studied in time, it seems fairly consistent. The displayed values are about what is expected, based on studying a large amount of discharges. Studying the second figure from the top, the Grad-Shafranov error, it can be seen that the calculation went well.

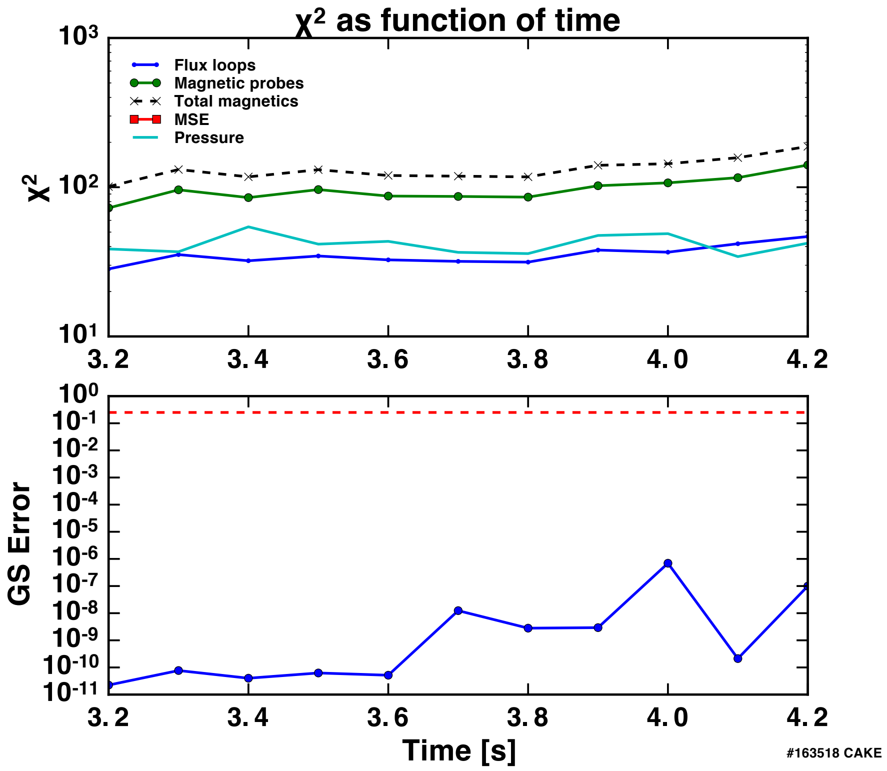

Figure 3.12: Top figure: χ^2 calculation of the different constraints fed to EFIT. Bottom figure: Grad-Shafranov error in time. The code aims for a converge of 1×10^{-8}. Results smaller than 1×10^{-4} are accepted, while larger values indicate issues.

3.3 Direct Criterion of Newcomb (DCON)

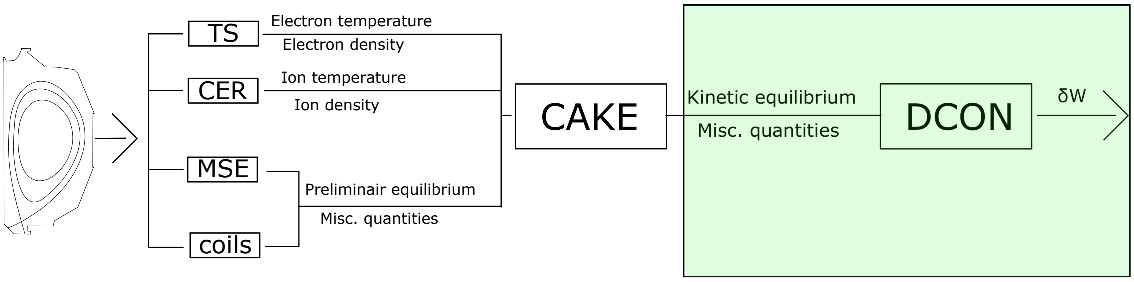

Figure 3.13: Overview of the experiment, diagnostics and codes used to calculate δW. Data moves from left, DIII-D reactor, to the right by 4 types of diagnostics and the CAKE / DCON codes.The green shaded area shows the part that is being discussed in this section.

DCON takes the output from a plasma equilibrium, in this work the output from CAKE, and applying a test-function to it which fits the boundary conditions and makes δW negative. The conditions the test function needs to satisfy is the integrating of a second order ODE, applying the Euler-Lagrange equation for the minimization of the potential energy and verifying if the result changes sign between singular points. This method, proposed by Newcomb, entail the Direct Criterion of Newcomb (DCON) and can be used to study the ideal MHD stability of a plasma. The output for DCON is δW, which is the change in total stored energy if the plasma gets perturbed for the least stable mode.

3.3.1 Running DCON

CAKE and DCON can be combined, starting from the input diagnostics and ending with a value for δW. This subsection show the example of two cases: a stable discharge and an unstable discharge.

The stable discharge, 163518, is studied from 2000ms to 4000ms and the unstable discharge, 150312, is studied from 2000ms to 3200ms. From both shots, 4 important properties have been plotted during their studied intervals. These plots can be seen in figure 3.14. The top figures are the total stored energy as a function of time, followed by the root mean square of the signals of the Mirnov coils on the $n = 1$,$n = 2$ and $n = 3$ mode numbers respectively. Looking at the stable shot, it can be seen that there are no islands present during the stable period and that the total stored plasma energy is consistent throughout. The unstable shot however has two important events. First, around 2500ms, a large spike can be seen on $n = 1$,$n = 2$ and $n = 3$ signals. The total stored plasma drops to half its total value. An event happened that caused the loss of confinement of a significant portion of the plasma. The discharge however recovers until a large tearing mode appears at 3000ms. During the formation of this island, half the stored energy is lost again.

For both shots during the discussed time intervals CAKE has reconstructed a kinetic profile every 5ms with an averaging window of 50ms. These results are given to DCON, which gives results for the ideal MHD calculation. These results can be seen in figure 3.15.

Looking at the left figure, displaying the stable results, it can be seen that δW is indeed positive and does not seem to vary much. Looking at the unstable discharge, different behavior can be seen. During the first 1/3th of the shot, when the plasma is stable, stable behavior is witnessed. However, right before the first collapse, δW starts to scatter. After the plasma stabilizes, the plasma remains scattered and scatters even more right before the final collapse.

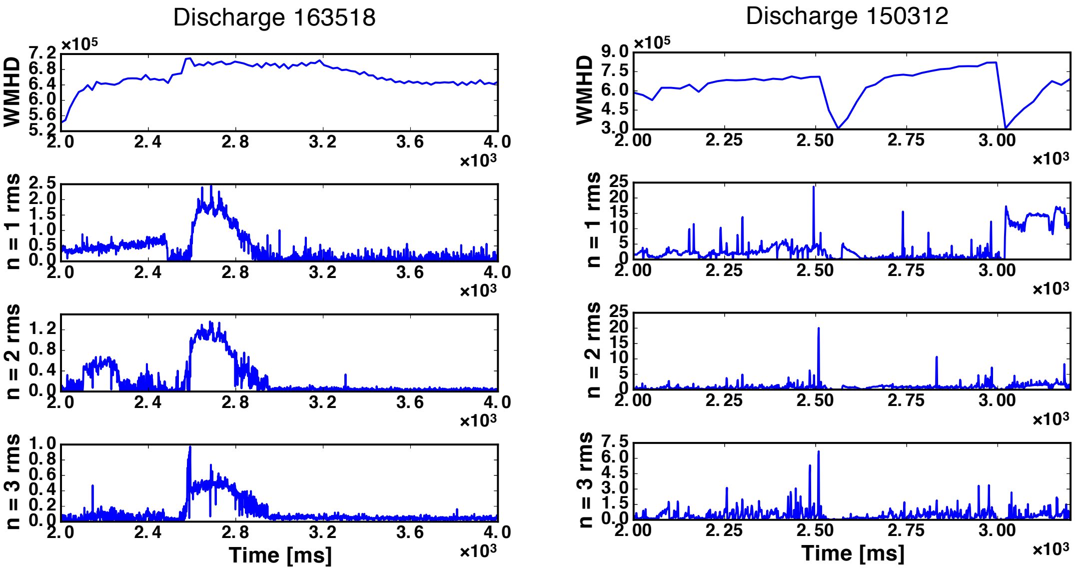

(a) 163518 from 2000 to 4000ms

(b) 150312 from 2000 to 3200ms

Figure 3.14: Figures (a) and (b) display, from top to bottom, total stored plasma energy and the n1rms, n2rms and n3rms time traces of the Mirnov coils. Figure (a) shows discharge 163518 during a stable period. The Mirnov coils show no large spikes and the total stored plasma energy does not fluctuate. Figure (b) shows unstable discharge 150312 where two large drops in the total stored plasma energy can be seen. The first one happens after a large spike in the Mirnov coil data while the second one happens right before a 2/1 island appears, characterized by the increase in the top Mirnov signal.

The plasma is ideal MHD stable, but before a tearing mode appears or a disruption happens, the value of δW starts to scatter. It should be noted that the onset of tearing modes is something that can be explained when studying resistive MHD and not with ideal MHD. How can this be explained?

Looking at the results in figure 3.15 something is missing: uncertainty. Keeping in mind that the input data for CAKE already has significant uncertainties and that there is additional uncertainty introduced due to Monte-Carlo processes in the code, it can be expected that the results from DCON also have uncertainties in them. If the uncertainties are very large it will be impossible to conclude anything about the results from DCON in combination with CAKE. The next chapter will use unscented transform to find the mean and variance of δW.

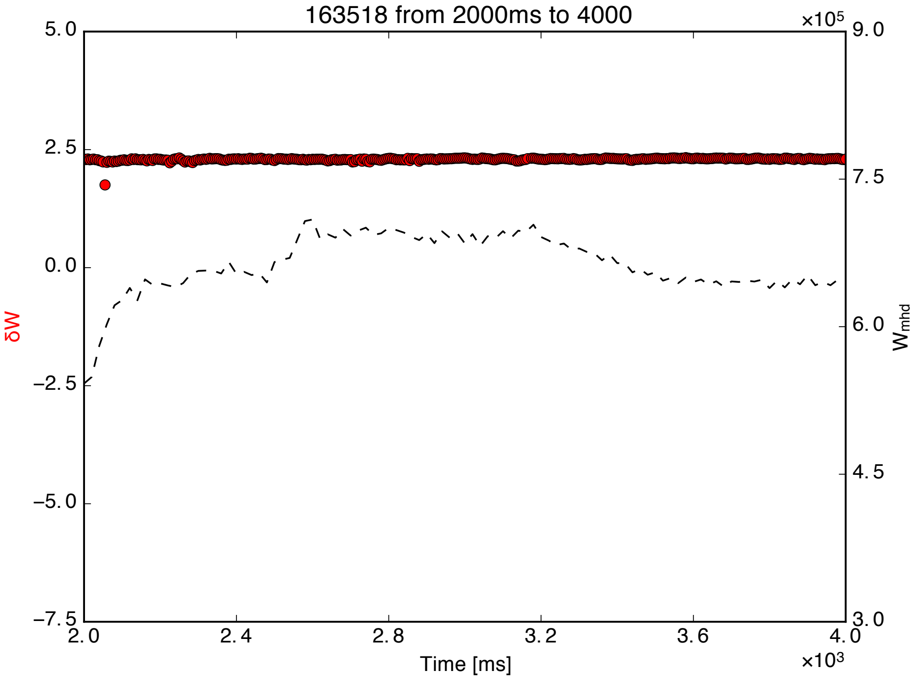

(a) 163518 sampled every $5ms$

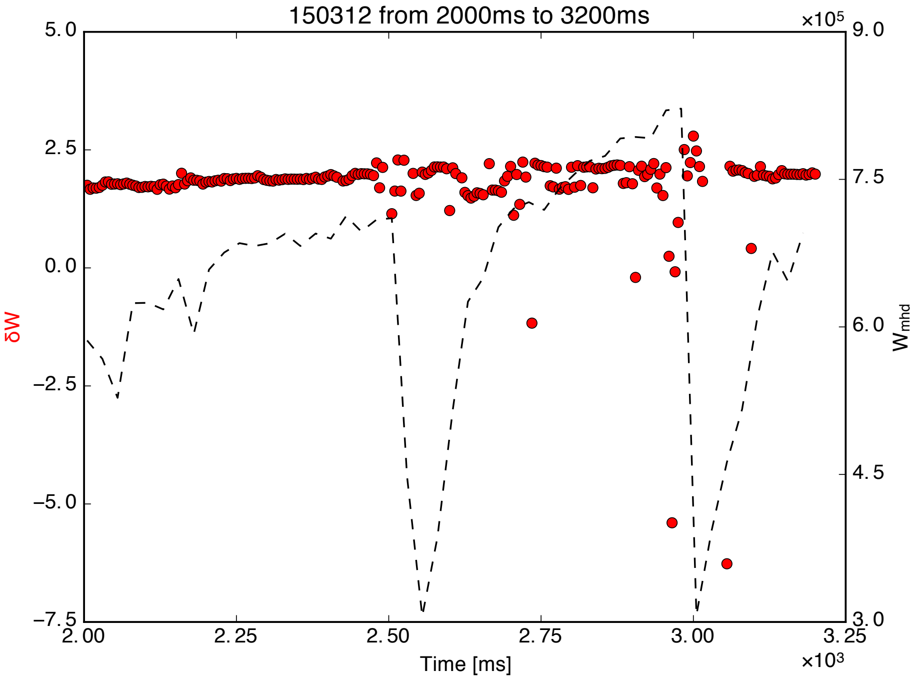

(b) 150312 sampled every $5ms$

Figure 3.15: Results from DCON as a function of time. Left: a stable plasma indeed shows consistent result. Right: After a large β_n collapse, noticeable by the drop in total stored energy W, a plasma is still present. After the second large dip of W a tearing mode is present that eventually kills the plasma. It can be seen that after the first drop, results from a δW show scattered behavior. This becomes more extreme as the tearing mode is approached.

3.4 Impact of diagnostics on ideal MHD calculations

The addition of various diagnostic data to reconstruct the plasma equilibrium could have a significant effect on the ideal plasma stability calculation. Comparing δW for various discharge types and different diagnostic configurations can give insight in this. Understanding this behavior makes it possible to indentify which diagnostic equipment is necessary and if this depends on the discharge scenario.

3.4.1 Constructing shot database

To get a broad spectrum of different shots, four types of inductive plasma scenarios have been chosen. From these scenarios, two discharges will be studied for 1000ms, using a 50ms interval and averaging window. An averaging window of $50ms$ has been chosen since this guarantees enough data for representative fitting while having a high enough temporal resolution to see stability effects. For one discharge type, the Super-H mode, 200ms will be studied with an interval of 10ms, since there are no discharges yet where a 1000ms Super-H mode has been maintained.

The first type of discharge is the 'ITER baseline scenario' (IBS) shot. Sawtoothing can be witnessed during H-mode due to a relaxed q-profile in combination with a low edge localized mode (ELM) frequency. The low injected power gives a relative low β_N of about 1.8 in DIII-D.

The second shot type is the 'Quiescent H-mode', or QH-mode. In these types of discharges the edge shear of the radial electric field is high, causing an edge harmonic oscillation to enhance transport. Rotational shear drives an unstable kink-peeling mode while the pedestal is kept below the MHD stability limit resulting in an absence of ELMs. Currently only the DIII-D tokamak has successfully ran this scenario.

Once access to the QH-mode has been achieved, it is possible to reach the third type of shot: 'Super H-mode'. Due to the high triangularity of this regime it is possible to access a stable regime. Sustaining the super H-mode for a long time remains difficult.

The 'Hybrid scenario' is the fourth type of shot. This shot is characterized by high stability, good confinement and the plasma is very stable compared to other scenarios. Sawteeth are absent, due to q being larger than 1. There is, however, a (small) $n = 2$ or $n = 3$ tearing mode present and the good confinement is lost at low rotation.

Shot	Type	Begin Time	End Time	Interval
153340	Super - H	3500	3700	10
153439	Super - H	4500	4700	10
162866	Hybrid	3000	4000	50
164613	Hybrid	2700	3700	50
172212	QH	2500	3500	50
172214	QH	2500	3500	50
173736	IBS	3500	4500	50
173740	IBS	3500	4500	50

Table 3.1: Discharges used for comparison

All discharges will be studied at the flat-top, when there are no large tearing modes or other anomalies present. Table 3.1 shows the list of discharges that has been used for comparison.

3.4.2 Comparing ideal MHD of different diagnostic setups

Now that the list of discharges has been chosen, the following equilibria need to be calculated for each shot: CAKE, CAKE without MSE, CAKE without CER, CAKE without CER and MSE and EFIT03.

The goal now is to show how much these setups differ from CAKE. Plotting the relative error, which is defined in equation 3.8, can be found in figure 3.16.

$$e = \frac{\delta W_{compare} - \delta W_{CAKE}}{\delta W_{CAKE}} \tag{3.8}$$

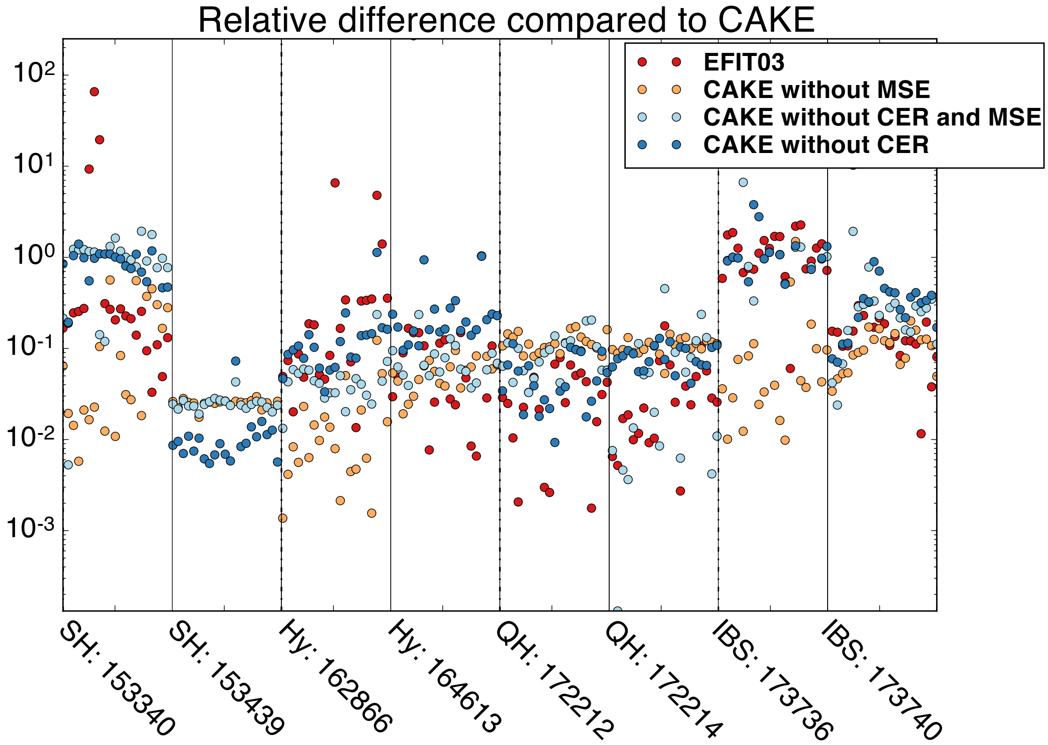

Figure 3.16: Relative error of the 8 discharges studied. Four different types of scenarios have been included which are ran the most in DIII-D. It can be seen that the absence of CER has the largest effect on the profile, except for the QH-scenario and the second Super-H discharge where the absence of MSE influences the results significantly.

Looking at this figure, a few things can be noticed. From the first two discharges, both Super H-mode discharges, the results are mixed. The first discharge, 153340, shows that CAKE without CER has very different results from CAKE. CAKE without MSE performs best and regular EFIT performs second best. The second Super H-mode discharge shows peculiar behavior: there are no extreme outliers and the absence of CER has almost no effect. Results have been verified and recalculated, but at the time of writing no explanation can be given for this behavior.

The next four shots show expected behavior. There is a clear difference between time slices. It shows that the computations where CER isn't used have the largest deviation from CAKE. It seems that CAKE without MSE preforms significantly different in the QH-shots than it does in the other discharge types. A reason for this could be that the core constraints MSE provide for the current density are significantly different from what is calculated by the Ohmic current estimation.

It can be concluded that different discharge scenarios need different diagnostics for optimal results. If it is assumed that the combination of all diagnostics provide the best result (CAKE), it can be seen that the absence of CER usually has the biggest effect on ideal MHD stability. The exception is in QH-mode, where the absence of MSE has the largest effect and one of the Super-H discharges. The absence of MSE, except for QH discharges, has overall the least effect and shows that the combination of TS, CER and magnetics at DIII-D is doing well at predicting ideal MHD stability even if most of the data is gathered in the pedestal.

Chapter 4

Unscented Kalman filter: application of CAKE and DCON

In this chapter the theory, code and diagnostics will be combined to design an algorithm that predicts the onset of tearing modes by studying ideal MHD stability. A database of discharges is constructed that all end in a tearing mode. Unscented transform will be applied to determine the uncertainty of δW. Validity of these results will be discussed by studying the influence of noise. Next, the unscented Kalman filter (UKF) is constructed using a random-walk model and will be tested on a basic case with a noisy non-linear function. After the dynamics have been discussed, the filter will be applied to three discharges at high temporal resolution. The goal is to see if it is possible to filter out computational noise and see if previously undetectable tearing modes can be detected.

4.1 Unscented transform of δW in time

For all the TS and CER channels the mean value and the standard deviation is known. As a result, it is possible to create the χ-vector for the unscented transform algorithm. Doing so for 10 discharges and 10 time slices for each discharge makes it possible to study the behavior of δW and its standard deviation in time. First, a database of shots will be constructed. For these shots the discharge type isn't important, the presence of a 2/1 tearing mode however is. It will be explained how the results from individual values for δW will be checked against 'faulty data' and how this is dealt with. The section about the application of unscented transform will be finished with a discussion about noise.

4.1.1 Database construction

For the purpose of studying the onset of tearing modes, shots will be picked that have a tearing mode after at least $1000ms$ of flat top. This allows 10 time slices to be studied while having a sufficient long time of stable behavior. No other requirements have been posed on the shot, except the presence of sufficient data CER and TS data so that the equilibrium can be reconstructed. The list of used shots can be found in 4.1 together with the maximum root mean square of the Mirnov-coil signal at n=1.

Shot	Tearing mode	Maximum n1rms
148791	4600	62.1
149415	4030	25.5
156746	4770	35.3
168832	4330	25.9
168887	3580	44.8
168899	3680	15.2
169591	2530	15.5
169595	2506	26.5
170125	2613	35.9
170219	4430	34.2

Table 4.1: Shots used for tearing mode analysis. Time for the start of the tearing mode has been included as well as the maximum RMS of the n=1 Mirnov signal of the following island.

From this list it can be seen that multiple shot types have been used, from various campaigns. The oldest shot, 147094, is from the 2011 campaign while the newest shot, 170219, is from 2017. The time where the tearing mode starts is determined as the first time an island grows and reaches a RMS of 10 on the n=1 Mirnov-coil diagnostic.

4.1.2 Applying unscented transform

By using unperturbed data, the equilibrium could be calculated and used as an input for DCON. To successfully apply the unscented transform algorithm, this calculation needs to be repeated many more times, each time perturbing a single property of a single diagnostic channel with a predetermined amount.

For every time slice and averaging window, the amount of active TS and CER channels can be determined. The standard deviation for the available data at that time is available, making it possible to calculate the χ-vector.

The χ-vector contains both the perturbations of the density and temperature of TS and CER data resulting in a vector with the following structure:

$$\chi = \begin{pmatrix} \mu_0 \\ \mu_0 + \sqrt{3}\alpha\sigma_{T_i} \\ \mu_0 - \sqrt{3}\alpha\sigma_{T_i} \\ \mu_0 + \sqrt{3}\alpha\sigma_{n_i} \\ \mu_0 - \sqrt{3}\alpha\sigma_{n_i} \\ \mu_0 + \sqrt{3}\alpha\sigma_{T_e} \\ \mu_0 - \sqrt{3}\alpha\sigma_{T_e} \\ \mu_0 + \sqrt{3}\alpha\sigma_{n_e} \\ \mu_0 - \sqrt{3}\alpha\sigma_{n_e} \end{pmatrix} \tag{4.1}$$

The vector has the dimensions of $(dat, 2 \times dat + 1)$ with dat the amount of active CER and TS channels during the studied timeslice. Variable μ_0 indicates the unperturbed data for all channels, α is a scaling factor and σ is the standard deviation of the perturbed quantity.

The scaling factor α determines how much data is sampled, see chapter 2. Using a scaling variable has an additional benefit: perturbing data too much may result in extreme deformations of the equilibria. This might result in interchange modes or violations of the Mercier criterion, rendering the results of δW unfeasible in some situation. This scaling parameter is set to be 0.1, Why this value is picked will be discussed in the subsection about the validity of the unscented transform.

Repairing data

The output from unscented transform needs to be repaired where necessary to maintain the full array size. Two types of faulty data can be distinguished: missing data and extreme negative values. Missing data can occur due to time-outs during the calculation or if the equilibrium is perturbed in such a way that DCON has difficulties calculating δW.

Extreme negative values, however, have a more physical meaning: it indicates the violation of the Mercier stability criterion, and means that the δW DCON computed is not reliable.

Before the data can be repaired, it is important to distinguish between incidental bad data or if it happens frequently. If either of the phenomena happen less for less than 5% of the calculations for a time-slice, it is considered incidental. Reasons for incidental computational errors can be due to server issues or performance issues with DCON. If this is the case, the corrupt data gets replaced with the average of the whole array without the corrupt data.

If the bad data does not happen incidental, it can be assumed that it is due to the perturbations of the plasma and it is no longer a computational error. As will be shown later, this is an indication that the plasma is close to forming a tearing mode. If this is the case, the repaired data gets calculated by:

$$\mathcal{Y}_i = \mu_{arr} - 2\sigma_{arr} \tag{4.2}$$

Here, $\mathcal{Y}_i$ is the value that gets repaired, μ_{arr} is the mean of the total array for that time slice without bad data and σ_{arr} is the standard deviation of that array. This method has been picked to make sure that the array can be kept at full length while also making sure that the repaired data indicates that the perturbation caused an unstable plasma.

4.1.3 Results of unscented transform

The 10 discharges that have been picked have been unscented transformed using the method discussed before. Settings for CAKE can be found in A while the settings for DCON can be found in appendix B. The results for discharge 170219 can be seen in figure 4.1 while the other 9 discharges can be found in appendix C. Three figures have been plotted, the top graph is δW in time with an error bar plotted in it. The error bar is defined as the standard deviation of δW divided by the mean value of δW for the corresponding time slices. The second figure from the top is a plot that shows the standard deviation as a function of time. The bottom graph are the time traces of the n1rms and β_n signals in time. In all three figures the shaded green areas display the averaging window, the time slice studied lies exactly in the middle of it. The red vertical line depicts where the tearing mode starts, as defined in the subsection about database construction.

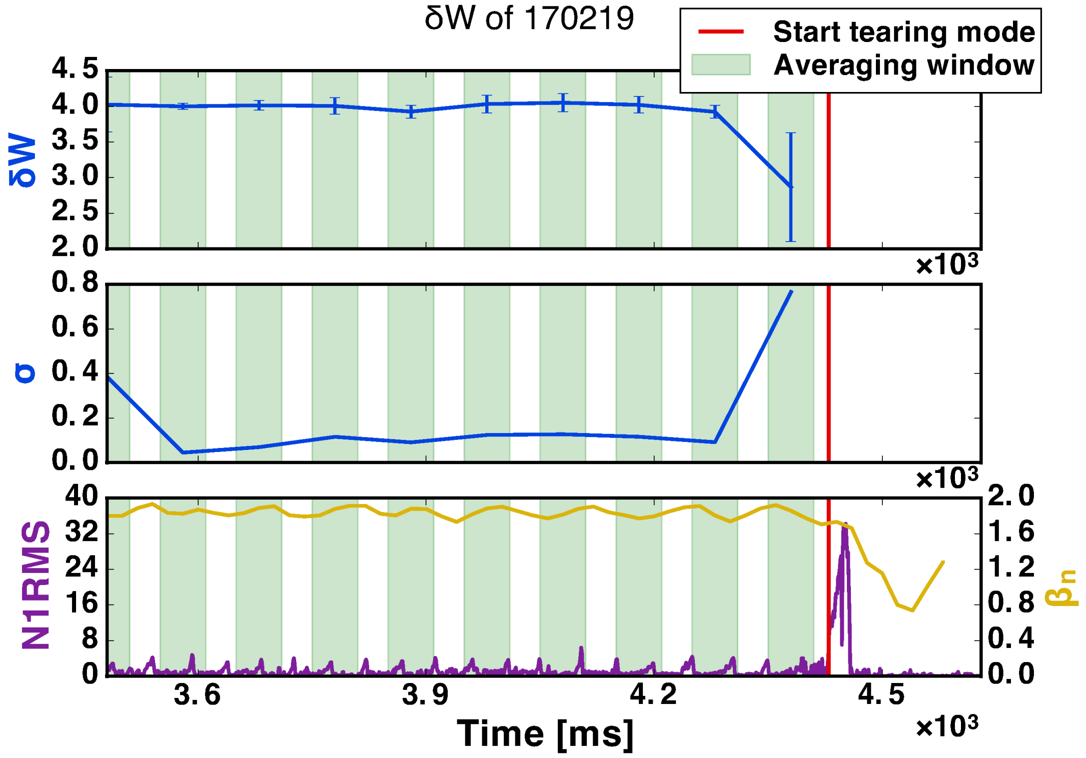

Figure 4.1: Calculation of δW in time including errorbar. Top: δW having an errorbar defined as $\frac{\sigma}{\mu}$. Middle: σ. Bottom: Normalized pressure β_n and the RMS of the $n = 1$ Mirnov signal. It can be seen that when the tearing mode, denoted by the red line, is approached the standard deviation increases significant. The green area denotes the time over which data has been averaged.

Looking at the result a few conclusions can be made. First of all, when the plasma is in a stable regime the standard deviation of δW is relatively small. If the plasma is ELMing, which can be seen by looking at small (< 5) spikes in the n1rms amplitude, the standard deviation is higher. We can conclude that these ELMs have a non-negligible effect on the equilibrium reconstruction. One reason for this could be that the presence of ELMs makes averaging more unreliable. A different answer for the increased standard deviation could be that the presence of ELMs increases the uncertainty on input data, causing the perturbations during the unscented transform to be larger.

An interesting phenomena is that in the cases where the maximum n1rms amplitude is larger than 26 of the final tearing mode, the standard deviation before the start of the tearing mode increases significantly, see table 4.2. It seems that the time it takes from the start of the tearing mode until the maximum has no influence on this effect, neither the scenario. The best example perhaps is shots 169191 and 169595, both are ran in the same proposal and are comparable shots. However 169191 does not show the increase in uncertainty before the start of the tearing mode while 169595 does. The biggest difference between the two is the maximum size of the island.

Shot	Tearing mode	Maximum n1rms	Increase σ_{dW}
148791	4600	62.1	Yes
149415	4030	25.5	No
156746	4770	35.3	Yes
168832	4330	25.9	No
168887	3580	44.8	Yes
168899	3680	15.2	No
169591	2530	15.5	No
169595	2506	26.5	Yes
170125	2613	35.9	Yes
170219	4430	34.2	Yes

Table 4.2: Discharges used for tearing mode analysis and their success

4.1.4 Validity of unscented transform

Two aspects need to be discussed to determine how reliable the results are: scaling of α and the influence of noise. The free parameter in unscented transform, α, determines how much the data is perturbed. Choosing it too large results in a perturbed equilibrium that can't be resolved by DCON. Picking α too small could result in a different problem: the result can be dominated by noise. Since there are multiple Monte-Carlo simulations in the CAKE code, there is a presence of noise. If α is chosen too small it could result in the problem that noise is becoming the dominant driving force in determining the uncertainty. By getting a sense for the upper and lower limit of α it is possible to discuss the validity of the unscented transform applied to CAKE.

Scaling of α

As discussed in the theory section, α determines the spread around the mean and is $0 < \alpha \leq 1$ as illustrated in figure 4.2.

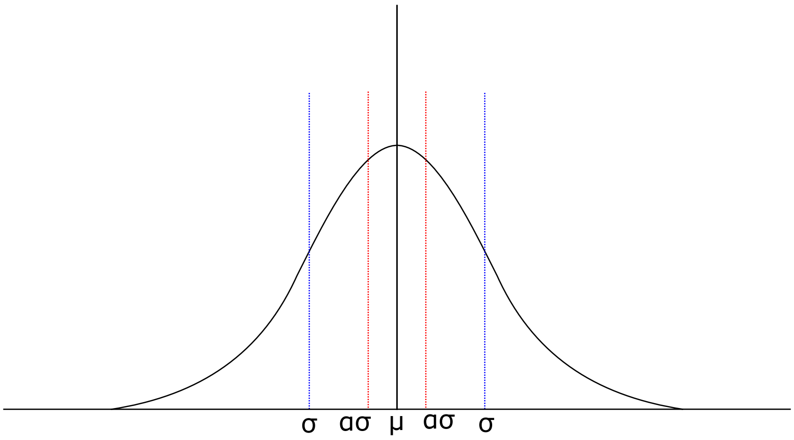

Figure 4.2: Schematic overview of α, standard deviation (σ) and the mean (μ). When α is picked as $0 < \alpha \leq 1$, the perturbations applied to the original corresponds to the red lines.

Picking α too small can in result the situation where the perturbation is relatively small compared to noise, while a large α can result in perturbations to the data that distort the equilibria too much for them to be used as input for DCON. To show the effect, the unscented transform algorithm has been used for shot 170219 for 5 values of α: 0.01,0.05,0.1,0.5 and 1. Plotting the amount of faulty data for these values of α in time results in figure 4.3.

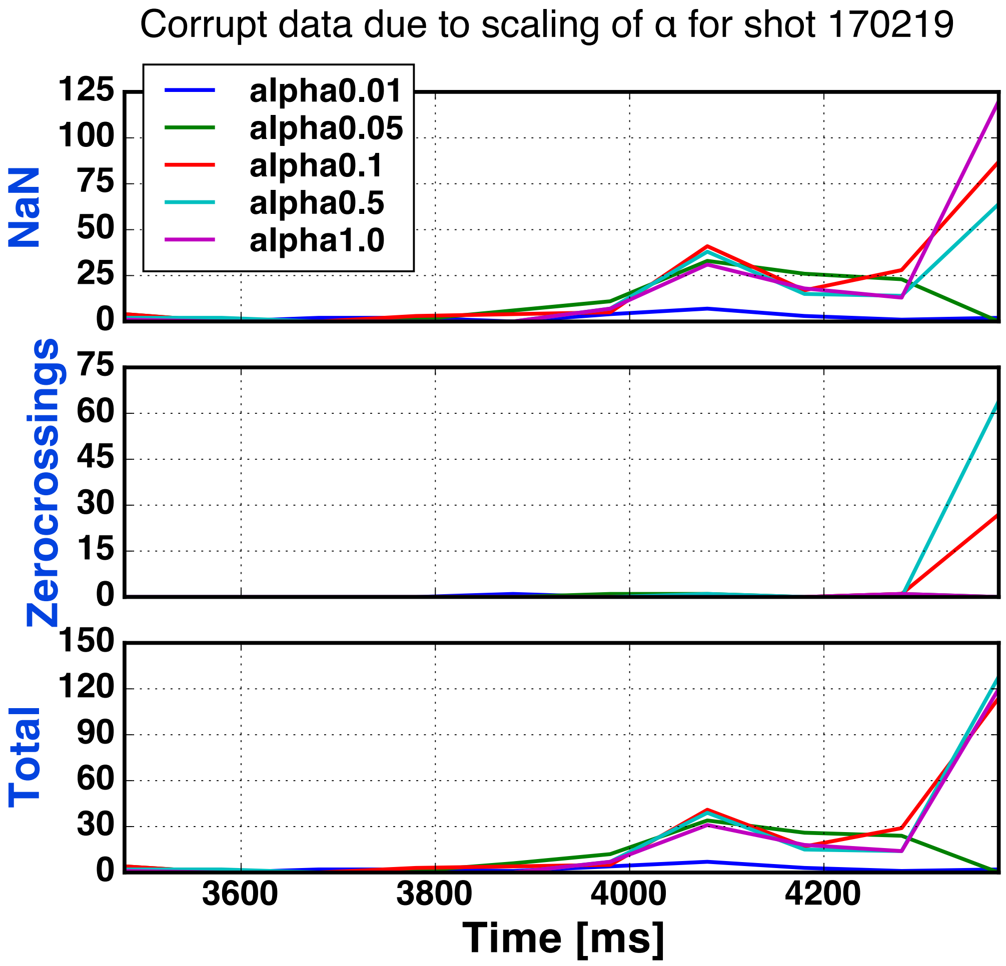

Figure 4.3: Overview of faulty data for shot 170219 as it nears a tearing mode. The top figure shows the amount of NaN's in the data set. It can be seen that when the tearing mode is approached, the large values for α show a large increase in unsuccessful DCON calculations. The second figure shows the amount of zero crossings that result in extreme values. Here it can be seen that this is not related to the size of α as the smallest and largest value do not show a large amount of zero crossings errors while the middle values do. The bottom figure shows the total faulty data.

From these results it can be seen that for large values of α, the amount of faulty data significantly increases when a tearing mode is approached. This can especially be seen in the NaNs, getting up to roughly 40% of corrupt data near the tearing mode for large values of α.

As a rule of thumb we can state that an α as small as possible is preferred. There is however a much harder lower limit on α as will be shown next.

Noise

During the fitting of the ion temperature, Monte-Carlo techniques are used for the optimal result. To study the effects of the resulting noise, it is possible to run the calculation for δW hundreds of times and study the standard deviation.

The results of such a calculation can be found in figure 4.4. Three standard deviations have been plotted in time for shot 170219, but each with varying values for α. The noise has also been plotted as the fourth function. From this it can be seen that for small perturbations, there is no clear distinction between noise and perturbed results. Only starting from $\alpha = 0.1$, a significant difference can be seen. This α will be used since this gives the least amount of corrupt data while still showing a significant difference from the noisy signal.

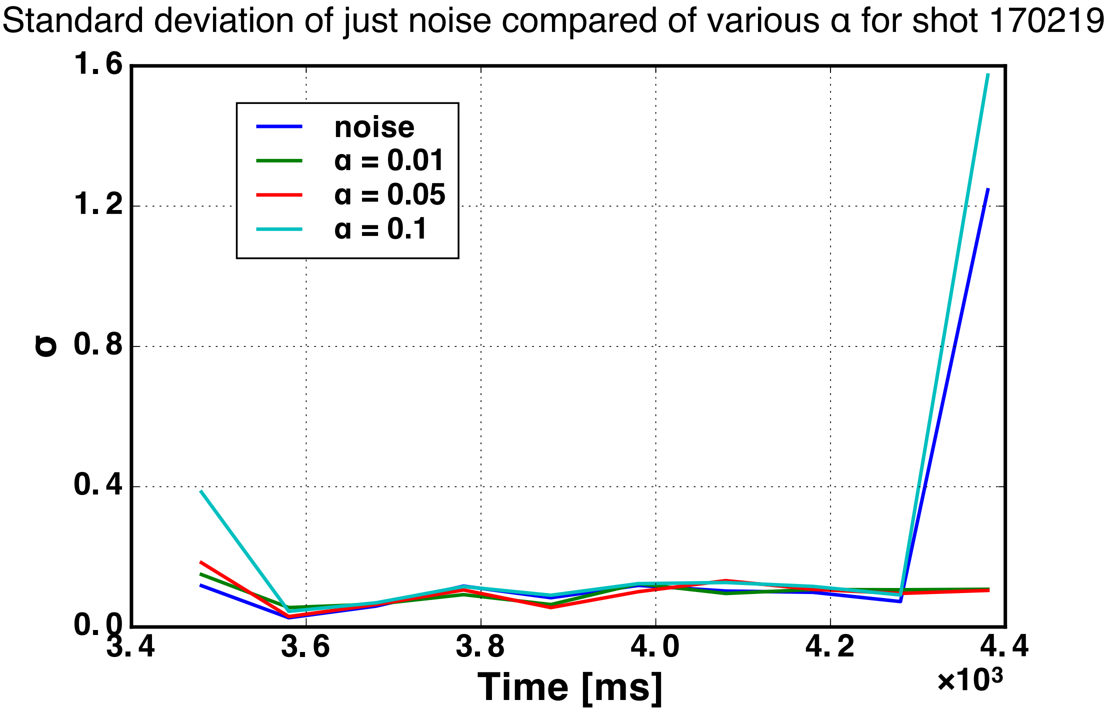

Figure 4.4: Results from unscented transform for various values of α and noise. It can be seen that if α is picked too small, the standard deviation is smaller than a simulation with just noise would be. Picking $\alpha = 0.1$ shows enough contrast near the tearing mode to be sure that the process is not noise dominated.

4.2 Unscented Kalman filter

While the results from the previous section seem good enough to apply directly, a sampling rate of 100ms only works if the start of the tearing mode is known beforehand. To do real detection, a higher temporal resolution is needed, so the tearing mode does not go unnoticed. Due to the presence of noise and sub-optimal data quality at higher time resolutions, it is important to start filtering the data to get a reliable result.

The chosen filter is the unscented Kalman filter (UKF), since the system is non-linear and the standard deviations of the process noise or measurement noise are not required as an input. To construct an UKF a model of the system needs to be included. Since a model is not present yet, a random walk model will be used. The requirements for a successful model will be discussed as well as what the random walk model means for the behavior of the UKF.

4.2.1 Model

The system can be written in a state space representation. To do so, it is important to determine the states, the relevant functions and to determine which noise is present. First, it can be assumed that the system that is being described is non-linear. The standard state space equations for a system with non-linear dynamics are:

$$\mathbf{x}_{k+1} = \mathbf{F}(\mathbf{x}_k, \mathbf{u}_k, \mathbf{v}_k) \tag{4.3a}$$

$$\mathbf{y}_k = \mathbf{H}(\mathbf{x}_k, \mathbf{n}_k) \tag{4.3b}$$

The state vector, $\mathbf{x}_k$, can be described as a non-linear function of $\mathbf{F}$ that is dependent on the previous state, an input $\mathbf{u}_k$ and noise $\mathbf{v}_k$. The observed measurement, $\mathbf{y}_k$, can be described by non-linear function $\mathbf{H}$ that depends on the state and the noise $\mathbf{n}_k$.

By picking the state to be the same as the measured output, it is possible to replace the non-linear function $\mathbf{H}$ by 1. Doing so means that the state of the system is the standard deviation of δW, σ_{dW}. The noise, n_k, is still present but is now added to the state:

$$\mathbf{x}_{k+1} = \mathbf{F}(\mathbf{x}_k, \mathbf{u}_k, \mathbf{v}_k) \tag{4.4a}$$

$$\mathbf{y}_k = \mathbf{x}_k + \mathbf{n}_k \tag{4.4b}$$

The nonlinear function $\mathbf{F}$ would be a model that makes it possible to evolve σ_{dW} in time as a function of inputs such as heating, fueling and magnetic configuration. Process noise is also present, this represents the noise on this system dynamics such as the uncertainties involved in the input data. Due to the absence of a model, a random-walk model has been used instead.

4.2.2 Algorithm

An algorithm has been proposed in chapter 2, and will be modified and applied in this chapter. The modifications that have been made are to get the correct internal state and the inclusion of the random walk model. The complete algorithm has been given below, a star in front of the equation means that it is a modification from the original algorithm:

$$\star \quad \boldsymbol{\chi}^{\chi}_{k-1} = ARRAY_{RAND}(\hat{\boldsymbol{x}}_{k-1}) \tag{4.5}$$

$$\star \quad \boldsymbol{\chi}^{\chi}_{k|k-1} = RW_x(\boldsymbol{\chi}^{\chi}_{k-1}) \tag{4.6}$$

$$\hat{\boldsymbol{x}}^-_k = \sum_{i=0}^{2L} W_i^{(m)} \chi^{\chi}_{i,k|k-1} \tag{4.7}$$

$$\hat{\boldsymbol{P}}^-_k = \sum_{i=0}^{2L} W_i^{(c)} \left(\chi^{\chi}_{i,k|k-1} - \hat{\boldsymbol{x}}^-_k\right) \left(\chi^{\chi}_{i,k|k-1} - \hat{\boldsymbol{x}}^-_k\right)^T \tag{4.8}$$

$$\star \quad \boldsymbol{\mathcal{Y}}_{k|k-1} = RN_y(\boldsymbol{\chi}^{\chi}_{k|k-1}) \tag{4.9}$$

$$\hat{\boldsymbol{y}}^-_k = \sum_{i=0}^{2L} W_i^{(m)} \mathcal{Y}_{i,k|k-1} \tag{4.10}$$

Measurement-update equations:

$$\boldsymbol{P_{y_k y_k}} = \sum_{i=0}^{2L} W_i^{(c)} \left(\mathcal{Y}_{i,k|k-1} - \hat{\boldsymbol{y}}^-_k\right) \left(\mathcal{Y}_{i,k|k-1} - \hat{\boldsymbol{y}}^-_k\right)^T \tag{4.11}$$

$$\boldsymbol{P_{x_k y_k}} = \sum_{i=0}^{2L} W_i^{(c)} \left(\chi_{i,k|k-1} - \hat{\boldsymbol{x}}^-_k\right) \left(\mathcal{Y}_{i,k|k-1} - \hat{\boldsymbol{y}}^-_k\right)^T \tag{4.12}$$

$$\mathcal{K}_k = \boldsymbol{P_{x_k y_k}} \boldsymbol{P_{y_k y_k}}^{-1} \tag{4.13}$$

$$\star \quad \hat{\boldsymbol{x}}_k = \hat{\boldsymbol{x}}^-_k + \mathcal{K}_k(\boldsymbol{UTF_{data}} - \hat{\boldsymbol{y}}^-_k) \tag{4.14}$$

$$\boldsymbol{P}_k = \boldsymbol{P}^-_k - \mathcal{K}_k \boldsymbol{P_{y_k y_k}} \mathcal{K}^T_k \tag{4.15}$$

One new variable and three new operations have been introduced. The variable, $\boldsymbol{UTF_{data}}$, is the result from the unscented transform calculation. The first operation, $ARRAY_{RAND}$ generates the χ-vector based on data from P_k and $\hat{x}$.

The other new operations is a random walk model (RW_x) and the addition of random noise (RN_y). The first random walk model represents the evolution of σ_{dW} in time as a function of inputs such as fueling or heating with the inclusion of noise.

$$\boldsymbol{\chi}^{\chi}_{k|k-1,i} = \begin{cases} \boldsymbol{\chi}^{\chi}_{k-1,i} + step_x, & \text{if } RAND \geq 0.5 \\ \boldsymbol{\chi}^{\chi}_{k-1,i} - step_x, & \text{otherwise} \end{cases} \tag{4.16}$$

The addition of random noise, RN_y, is achieved by generating random Gaussian white noise and adding this to the obtained result from the random walk model.

Testing

To show the algorithm works, a sine function can be combined with noisy data. Figure 4.5 shows the clean sine function in blue while noise has been additively added that results in the green noisy signal. Testing the algorithm by using the noise signal as the UTF_{DATA} from the algorithm, gives the new signal (red) in the same function.

It can be seen that even with the absence of a model and using random walk, some of the noise gets filtered out. In fact, the data that is filtered out is high frequent and a low-pass filter has

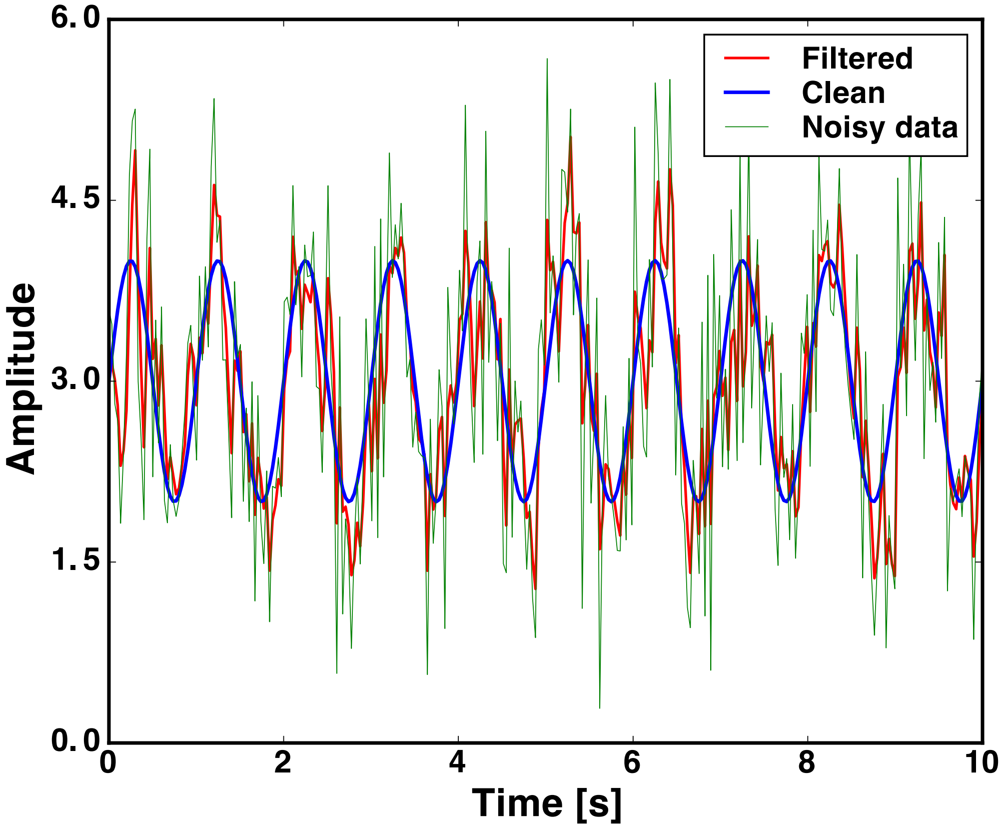

Figure 4.5: Basic case to test UKF: a clean non-linear function (blue) gets random noise which results in the noisy signal (green). Using the UKF with a random walk model, some of the noise gets filtered out and a cleaner signal is given (red).

been designed. High frequent dynamics get filtered out because the high frequent dynamics have a large variance. If the variance of the noisy data gets too large, the Kalman gain puts more weight on the random walk model instead. Figure 4.6 shows the normalized Fourier transform of all three signals. It can be seen that at low frequent behavior both the noisy and the filtered data are the same, but at higher frequencies the results start to differ.

Since the dynamics are as expected, a low pass filter, and it has been successfully tested on a theoretical example it is possible to conclude that a low pass filter has been successfully created and it is plausible that the algorithm is working as intended.

4.2.3 Application of UKF on a real case

Three shots have been studied at a higher temporal resolution: discharge 163518, 156746 and 149415. The first discharge has no tearing modes and will be studied during a period where β_N is almost constant. The second discharge does have a tearing mode that has been detected successfully. The third discharge also ends in a tearing mode, but was not successfully detected by just using unscented transform. A total of 40 samples will be taken with an interval of 20ms. The

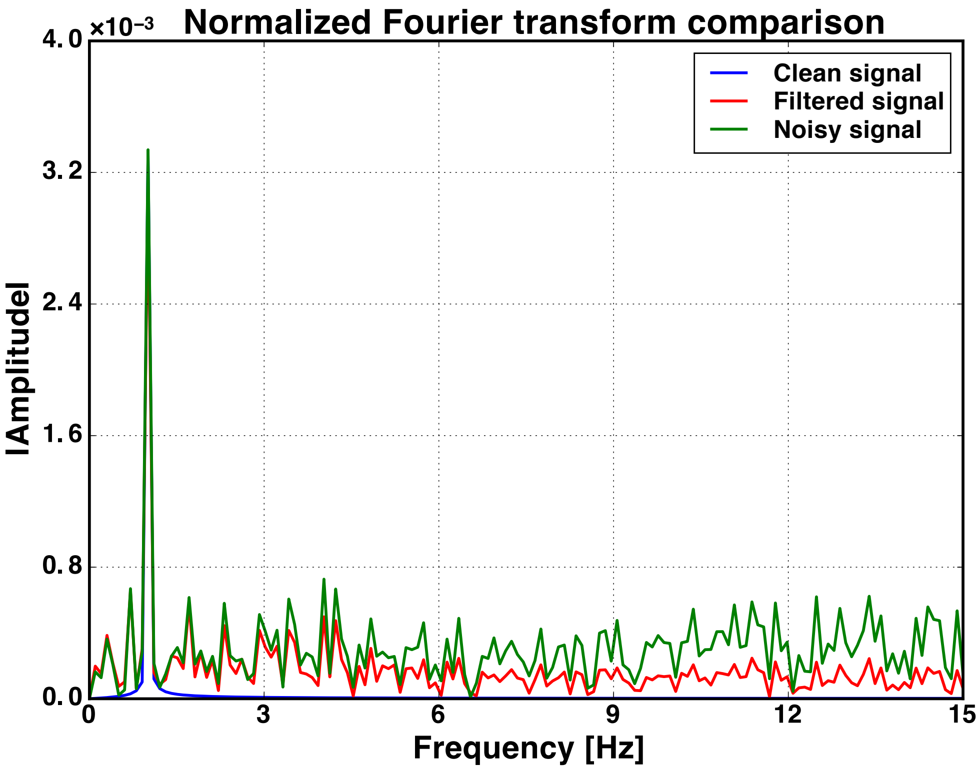

Figure 4.6: Normalized Fourier transform of the three signals. The clean signal shows indeed a peak at 1Hz while the noisy signal shows additional noisy behavior. At low frequencies the noisy data and filtered data behave the same but at higher frequencies it can be seen that the filtered signal is suppressing high frequent noise.

results of the unfiltered case are shown in figure 4.7. Here it can be seen that the noisy behavior can give misleading results: while there is indeed an increase of σ_{dW} before the onset of the tearing mode, there is also a decrease (156746) and the stable discharge shows one large spike. If this is indeed the result of high frequent noise, the UKF should be able to filter this out.

Looking at figure 4.8 it can be seen that the results are indeed better. The stable discharge, 163518, shows no longer any extreme outliers. The unstable discharge, 156746, shows a clear increase right before the tearing mode now that a peak caused by high frequent behavior is gone.

For the cleaning of noise, it can be seen that a simple low pass filter would work sufficiently: by removing high frequent noise the results become much more clear. However, is this also sufficient to detect the onset of tearing modes that where not detectable before?

Studying discharge 149415, where the detection failed, it can be seen that this is not the case. Figure 4.9 shows the result, and it can be seen that there is no large increase in σ_{dW} before the onset of the tearing mode. As a result, we can state that simply using a low pass filter will not work in designing a detector that predicts all tearing modes.

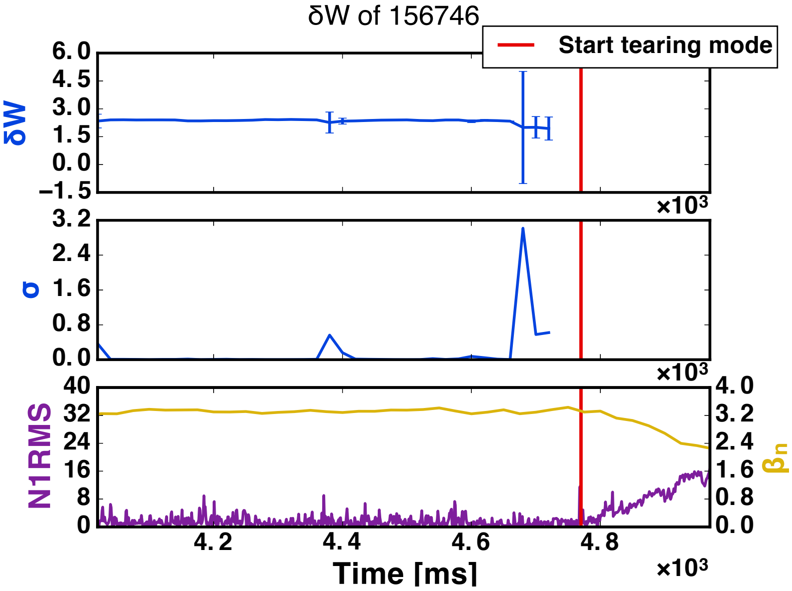

(a) 156746 sampled every $20ms$

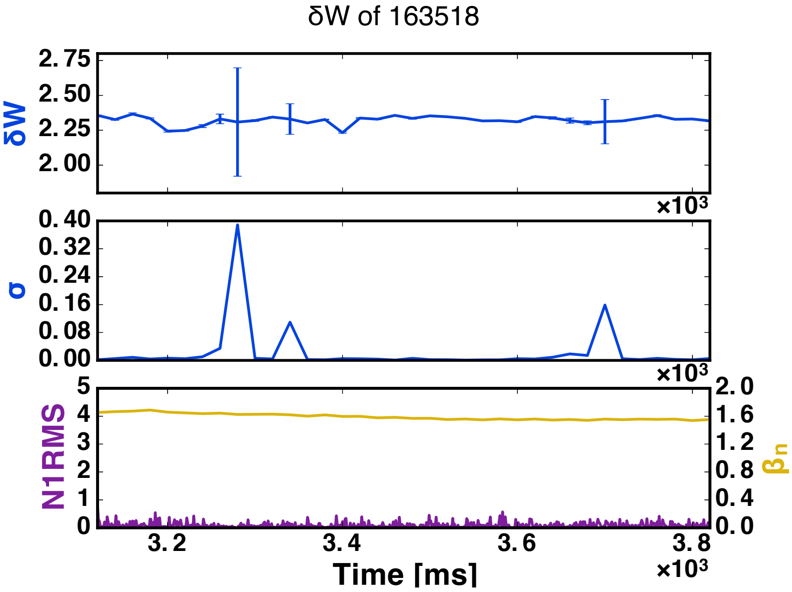

(b) 163518 sampled every $20ms$

Figure 4.7: High temporal resolution scans of discharge which tearing mode was predicted successfully (a) and a stable discharge (b). In both discharges unexpected spikes in the standard deviation can be witnessed.

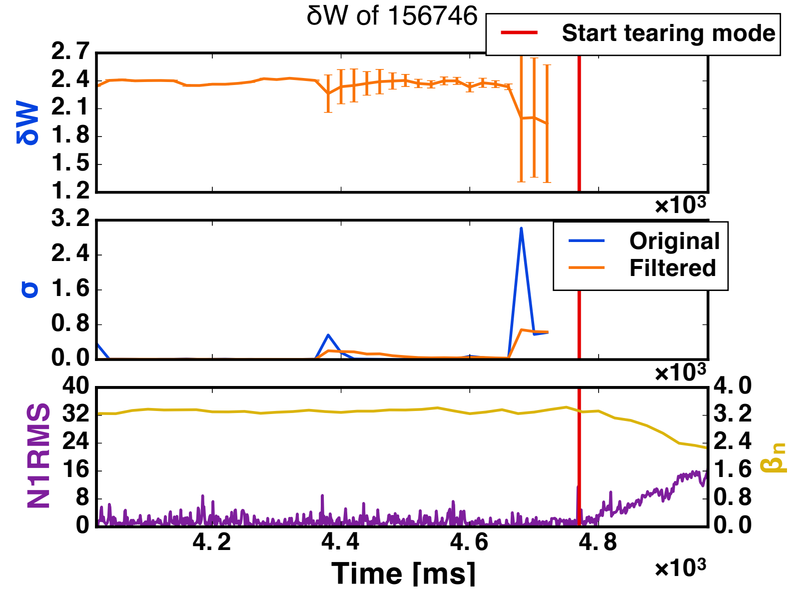

(a) 156746 sampled every $20ms$

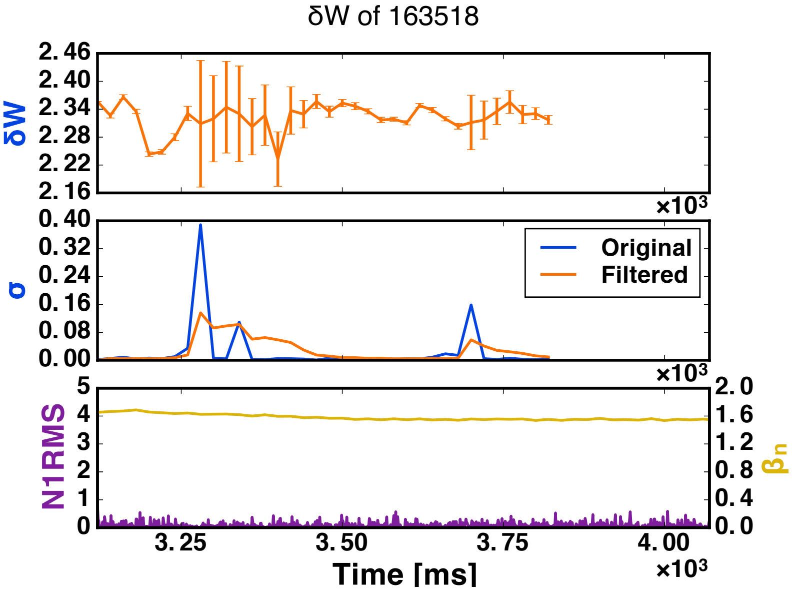

(b) 163518 sampled every $20ms$

Figure 4.8: Filtered high temporal resolution scans of discharge which tearing mode was predicted successfully (a) and a stable discharge (b). The unexpected spikes have disappeared resulting in relative constant behavior for the stable discharge and a more clear result for the discharge that ended in a tearing mode.

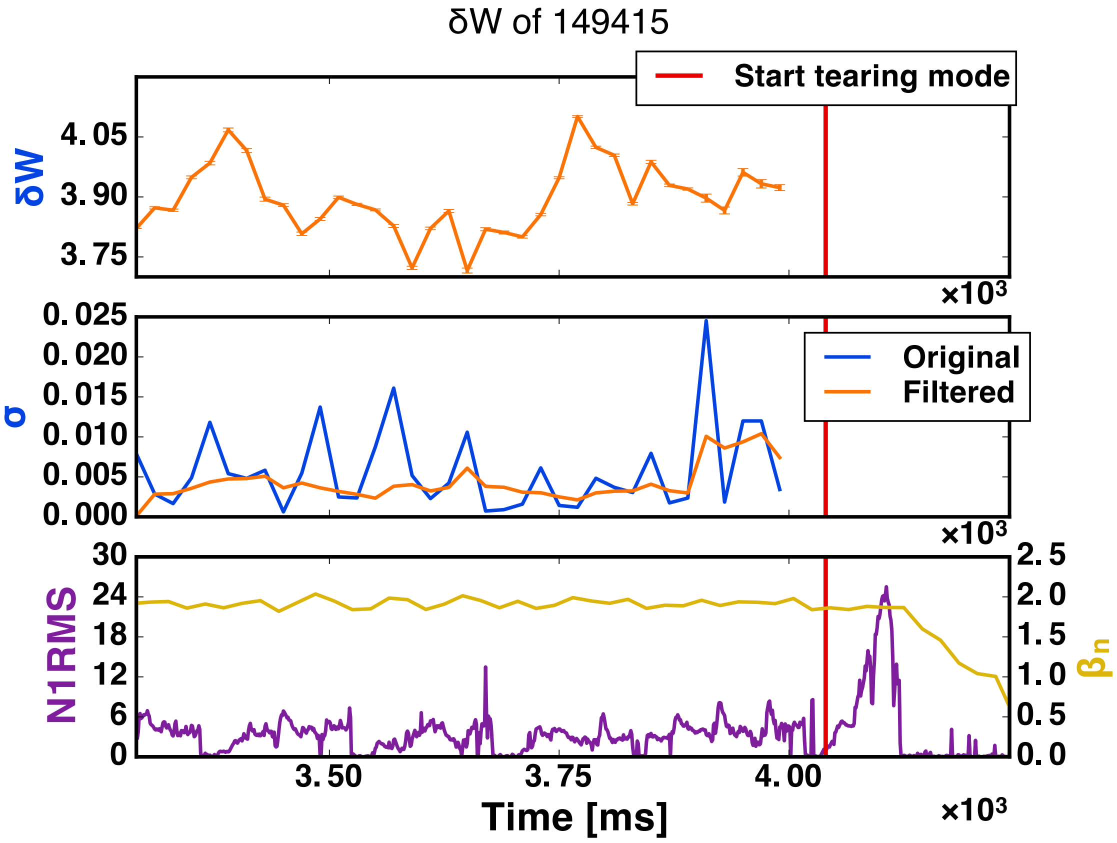

Figure 4.9: Using the unscented Kalman filter with a random walk model does not improve the capability of detecting the tearing modes: there is no significant increase in σ_{dW} before the tearing mode, even when the data is filtered.

Chapter 5

Conclusion and Discussion

The goal of this work was to develop an algorithm that is able to predict tearing modes by studying ideal MHD properties of the plasma. As a result, the following research question was posed:

Is it possible to predict the start of a tearing mode by calculating the uncertainty of ideal magnetohydrodynamic calculations?

After analyzing ten discharges it could be seen that if the tearing mode would grow to at least a size that corresponds to a root mean square of 26 for the $n = 1$ Mirnov coil a tearing mode could be predicted if the standard deviation of the ideal MHD equation is analyzed. Around $20ms$ before the onset of a tearing mode, the standard deviation becomes significantly bigger, corresponding with small perturbations on the input data having a large effect on the plasma equilibrium.

The standard deviation of δW can be determined by using a so-called 'unscented transform' on the output of CAKE and DCON. CAKE is being used to collect diagnostic data from DIII-D and create a kinetic equilibrium, a high quality equilibrium that has physical features such as the pedestal. DCON takes the reconstructed equilibrium and determines δW of this equilibrium. By perturbing the input data of CAKE, it will be able to get a wide range of values for δW for a certain time slice. This can be reconstructed in to the mean and standard deviation of δW.

While it has been discussed that there is a small error due to noise, the noise has an additional effect: scaling parameter α might influence the results. The scaling parameter is introduced as a tool to prevent domination of high-order terms, and can be seen as a way of limiting how much of the input standard deviation should be taken in to account. If α is picked too small, noise in the process due to Monte-Carlo simulations will dominate the process while an α thats perturbs the equilibrium too much makes DCON not able to compute the ideal MHD properties.

The results from the unscented transform contain noisy results due to bad data. As a result, it is useful to filter the data. By using a model-based filter it is possible to include a model which could improve the state-estimation performed by the filter. An unscented Kalman filter has been picked for this role due to the expected non-linear behavior of the system and the fact that it does not need the standard deviation of the process and measurement noise as an input.

Studying three shots in high temporal resolution (20ms interval) shows that the unscented Kalman filter is able to filter out some of the high frequent noise, making the results much clearer. The unscented Kalman filter however does not make possible to detect previously undetectable tearing modes (n1rms ≤ 26).

Two subquestions have been posed that where needed to come to the previous conclusions. The first one is:

Does the Consistent Automatic Kinetic Equilibrium (CAKE) solver provides accurate kinetic equilibria?

A new tool for the reconstruction of kinetic equilibria has been introduced: CAKE. It has been shown how the code works for DIII-D and when to trust the results. Since a direct comparison with experiments is not possible, two measures of error should be analyzed to see how good the equilibrium is: the Grad-Shafranov error and the χ^2-error. The former is a measure how well the imposed constraints match the solution while the latter is a measurement how well the final result corresponds with the original input data. If both errors are small, the results are considered good. Using the tool extensively shows that results are only poor if there is lack of data or a wrong time interval is picked where the plasma cant be considered ideal.

The next subquestion focuses on the determination of the uncertainty in the ideal MHD calculation.

Can the uncertainty be determined of the ideal magnetohydrodynamic stability calculation results from 'DCON'?

Exploiting the fact that it is possible to calculate a lot of kinetic profiles, it is possible to apply a so-called 'unscented transform'. This technique, that resembles a Monte-Carlo simulation, makes it possible to propagate a set of pre-determined perturbations through a non-linear function. One key advantage of using this technique is that it is possible to reconstruct the mean and standard deviation without knowing the mapping function between the in- and output.

This was implemented by perturbing the input data from each Thomson scattering channel and Charge Exchange Recombination channel by a fixed amount of its standard deviation. As a result it was possible to only run 200 stability calculations instead of the thousands that would be needed for the Monte Carlo results to converge.

Discussion

The filter and underlying techniques can be improved in several ways to improve performance. First of all, the CAKE code can be improved. The code has been developed with the idea that large quantities of profiles can be used to see underlying physical process due to statistical analysis. While the code indeed seems to be accurate enough for this, individual profiles lack details sometimes. One of the reasons for this is that the CER data is not corrected: much like TS data, the location of data can be off sometimes. Having discussed this option with the CER-group at General Atomics, no clear consensus could be reached on how to solve this. A quick and dirty solution would be to calculate the radial electric field near the edge and shift the CER such that the field is zero at the last closed flux surface. While indeed such a feature was implemented in CAKE, accuracy of the calculated radial electric field is still a point of controversy.

The unscented transform calculation also could be improved. While the theory is solid, only TS and CER data is perturbed at this time. For a complete picture, magnetics and MSE also need to be included. The downside of this would be that this would increase the computation time. This will however give a more complete picture of the whole process.

Even without extending the unscented transform parameters by adding magnetics and MSE, the calculation takes hours to complete for a single time slice. This is such a time consuming process that real-time capability will never be possible. However, two suggestions can be mode to speed up the process. First, it is possible to use only a tanh-fit for all the CER/TS parameters. Using a tanh-fit instead of a more sophisticated fit has the effect that the total fit is shifted up or down the same for each channel. This can be exploited to only run 8 calculations, all properties (4) in the negative and positive direction. This can then be multiplied with the amount of channels that actually have measured for a time to reconstruct what the output would be if all 200 channels would have ran. One clear downside of using this method is that the fits get worse in the pedestal region, but also effects like internal transport barriers can't be seen since the tanh-fit is a linear function in the core.

The second method to increase calculation speed is by just calculating the sensitivity to the process-noise. When the ONETWO-code is used for the fast ion calculations, and the most sophisticated fitting functions are used, there is process noise present in the equilibrium reconstruction by CAKE. While this noise is negligible during stable phases of the discharge, it is clearly present when a tearing mode is approached. While still an order of magnitude smaller than when perturbations are used, it is clearly distinguishable. Since the introduced noise has its own mean and variance, this can be detected and exploited to prevent tearing modes. It should be noted that when this method is used, all information is lost about the total effect of all the uncertainties in measurement data. It however makes it possible to run an amount of calculations that is in the order of 10 instead of 100, opening a possibility to parallelize the whole process and making real time application possible again.

Improving the unscented Kalman filter can be done by replacing the random-walk model by an actual model of the process. This could increase the performance a lot and could make it possible to detect all the tearing modes instead of only tearing modes of a certain size. While a complete model of the plasma is probably too extensive and makes real time analysis difficult, machine learning based models are being developed. While these models would teach us nothing about the physics that is going on, as long as all the inputs are taken in to account such as neutral beam injection and electron cyclotron current drive and the evolution of δW can be described in time with a standard deviation, it is expected that a large increase in performance of the filter could be achieved.

Bibliography

[1] D. J. C. Mackay, *Sustainable Energy without the hot air*, vol. 78. 2009.

[2] J. P. Freidberg, *Plasma Physics and Fusion Energy*, vol. 1. 2007.

[3] M. Kikuchi, K. Lackner, and M. Quang, "Fusion Physics," *Iaea*, pp. 24–26, 2012.

[4] P. Piovesan, V. Igochine, F. Turco, D. A. Ryan, M. R. Cianciosa, Y. Q. Liu, L. Marrelli, D. Terranova, R. S. Wilcox, A. Wingen, C. Angioni, A. Bock, C. Chrystal, I. Classen, M. Dunne, N. M. Ferraro, R. Fischer, A. Gude, C. T. Holcomb, A. Lebschy, T. C. Luce, M. Maraschek, R. McDermott, T. Odstrčil, C. Paz-Soldan, M. Reich, M. Sertoli, W. Suttrop, N. Z. Taylor, M. Weiland, and M. Willensdorfer, "Impact of ideal MHD stability limits on high-beta hybrid operation," *Plasma Physics and Controlled Fusion*, vol. 59, no. 1, p. 014027, 2017.

[5] G. Janeschitz, "Plasma wall interaction issues in ITER," *Journal of Nuclear Materials*, vol. 290, pp. 1–11, 2001.

[6] J. P. Freidberg, "Ideal magnetohydrodynamic theory of magnetic fusion systems," *Reviews of Modern Physics*, vol. 54, no. 3, pp. 801–902, 1982.

[7] R. Iacono, a. Bhattacharjee, C. Ronchi, J. M. Greene, and M. H. Hughes, "Stability of tearing modes in finite-beta plasmas," *Physics of Plasmas*, vol. 1, no. 8, p. 2645, 1994.

[8] D. P. Brennan, E. J. Strait, A. D. Turnbull, M. S. Chu, R. J. \mboxLa Haye, T. C. Luce, T. S. Taylor, S. Kruger, A. Pletzer, R. J. La Haye, T. C. Luce, T. S. Taylor, S. Kruger, and A. Pletzer, "Tearing mode stability studies near ideal stability boundaries in \mbox{DIII-D}," *Phys. Plasmas*, vol. 9, no. 7, p. 2998, 2002.

[9] D. A. Humphreys, J. R. Ferron, R. J. La Haye, T. C. Luce, C. C. Petty, R. Prater, and A. S. Welander, "Active control for stabilization of neoclassical tearing modes," *Phys. Plasmas*, vol. 13, p. 56113, 2006.

[10] D. A. Humphreys, J. R. Ferron, M. Bakhtiari, J. A. Blair, Y. In, G. L. Jackson, H. Jhang, R. D. Johnson, J. S. Kim, R. J. LaHaye, J. A. Leuer, B. G. Penaflor, E. Schuster, M. L. Walker, H. Wang, A. S. Welander, and D. G. Whyte, "Development of \mbox{ITER}-relevant plasma control solutions at \mbox{DIII-D}," *Nucl. Fusion*, vol. 47, p. 943, 2007.

[11] R. J. \mboxLa Haye, S. Günter, D. A. Humphreys, J. Lohr, T. C. Luce, M. E. Maraschek, C. C. Petty, R. Prater, J. T. Scoville, and E. J. Strait, "Control of neoclassical tearing modes in DIII-D," *Phys. Plasmas*, vol. 9, p. 2051, 2002.

[12] Y. Nishimura, J. D. Callen, and C. C. Hegna, "Tearing mode analysis in tokamaks, revisited," *Physics of Plasmas (1994- . . .*, vol. 5, no. 12, pp. 4292–4299, 1998.

[13] C. M. Bishop, J. W. Connor, R. J. Hastie, S. C. Cowley, R. J. H. C. M. Bishop, I. W. Connor, and S. C. Cowley, "On the difficulty of determining tearing mode stability," *Plasma Physics and Controlled Fusion*, vol. 33, no. 4, p. 389, 1991.

[14] C. C. Hegna and J. D. Callen, "Stability of tearing modes in tokamak plasmas," *Physics of Plasmas*, vol. 1, pp. 2308–2318, 7 1994.

[15] D. P. Brennan, R. J. La Haye, A. D. Turnbull, M. S. Chu, T. H. Jensen, L. L. Lao, T. C. Luce, P. A. Politzer, E. J. Strait, S. E. Kruger, and D. D. Schnack, "A mechanism for tearing onset near ideal stability boundaries," *Physics of Plasmas*, vol. 10, no. 5 II, pp. 1643–1652, 2003.

[16] I. B. Bernstein, E. A. Frieman, M. D. Kruskal, and R. M. Kulsrud, "An Energy Principle for Hydromagnetic Stability Problems," *Proc. Roy. Soc. A*, vol. 244, p. 17, 1958.

[17] A. H. Glasser, "The direct criterion of Newcomb for the ideal MHD stability of an axisymmetric toroidal plasma," *Physics of Plasmas*, vol. 23, no. 7, p. 72505, 2016.

[18] L. L. Lao, H. S. John, R. D. Stambaugh, A. G. Kellman, and W. Pfeiffer, "Reconstruction of current profile parameters and plasma shapes in tokamaks," *Nucl*, vol. 105, 1985.

[19] D. Eldon, E. Kolemen, M. A. Roelofs, and W. J. Eggert, "Development of an automatic kinetic equilibrium reconstruction workflow for tokamak plasma stability analysis,"

[20] S. Julier, "The scaled unscented transformation," *Proceedings of the 2002 American Control Conference (IEEE Cat. No.CH37301)*, no. 2, pp. 4555–4559, 2002.

[21] Julier and Uhlmann, "A new extension of the Kalman filter to nonlinear systems.," *Int. Symp. Aerospace/Defense Sensing, Simul. and Controls*, vol. 3, p. 26, 1997.

[22] H. Grad and H. Rubin, "Hydromagnetic Equilibria and Force-Free Fields," *Proceedings of the 2nd UN Conf. on the Peaceful Uses of Atomic Energy*, vol. 31, p. 190, 1958.

[23] M. S. Chance, "Vacuum calculations in azimuthally symmetric geometry Vacuum calculations in azimuthally symmetric geometry," vol. 2161, 1997.

[24] H. P. Furth, J. Killeen, and M. N. Rosenbluth, "FiniteResistivity Instabilities of a Sheet Pinch," *Physics of Fluids*, vol. 6, no. 1963, pp. 459–484, 1963.

[25] R. E. Kalman, "A New Approach to Linear Filtering and Prediction Problems," *Journal of Fluids Engineering*, vol. 82, no. Series D, pp. 35–45, 1960.

[26] J. L. Luxon, "A design retrospective of the \mbox{DIII-D} tokamak," *Nucl. Fusion*, vol. 42, p. 614, 2002.

[27] J. Luxon, "A Design Retrospective of the DIII-D Tokamak," *Nuclear Fusion*, vol. 42, no. 5, pp. 614–633, 2002.

[28] D. Eldon, B. D. Bray, D. M. Ponce, A. J. Chavez, T. M. Deterly, R. J. Groebner, C. Liu, T. H. Osborne, and P. B. Snyder, "High resolution pedestal \mbox{Thomson} scattering system at \mbox{DIII-D}." Poster presented at the 52nd meeting of the APS DPP in Chicago, IL, 2010.

[29] D. M. Ponce-Marquez, B. D. Bray, T. M. Deterly, C. Liu, and D. Eldon, "\mbox{Thomson} scattering diagnostic upgraded on \mbox{DIII-D}," *Rev. Sci. Instrum.*, vol. 81, p. 10D525, 2010.

[30] D. Eldon, A. G. McLean, T. N. Carlstrom, C. Liu, M. Watkins, B. D. Bray, E. Kolemen, R. J. Groebner, T. H. Osborne, P. B. Snyder, R. L. Boivin, and G. R. Tynan, "Maintaining, upgrading, and expanding the role of \mbox{Thomson} scattering at \mbox{DIII-D}." Invited talk presented at the 16th international symposium on Laser-Aided Plasma Diagnostics in Madison, WI, 2013.

[31] D. Eldon, B. D. Bray, T. M. Deterly, C. Liu, M. Watkins, R. J. Groebner, A. W. Leonard, T. H. Osborne, P. B. Snyder, R. L. Boivin, and G. R. Tynan, "Initial results of the high resolution edge Thomson scattering upgrade at DIII-D," *Review of Scientific Instruments*, vol. 83, no. 10, pp. 1–4, 2012.

[32] C. Chrystal, K. H. Burrell, B. A. Grierson, S. R. Haskey, R. J. Groebner, D. H. Kaplan, and A. Briesemeister, "Improved edge charge exchange recombination spectroscopy in DIII-D," *Review of Scientific Instruments*, vol. 87, no. 11, pp. 1–4, 2016.

[33] K. H. Burrell, P. Gohil, R. J. Groebner, D. H. Kaplan, J. I. Robinson, and W. M. Solomon, "Improved charge-coupled device detectors for high-speed, charge exchange spectrscopy studies on the \mbox{DIII-D} tokamak," *Rev. Sci. Instrum.*, vol. 75, p. 3455, 2004.

[34] D. Wróblewski and L. L. Lao, "Polarimetry of motional Stark effect and determination of current profiles in DIII-D (invited)," *Review of Scientific Instruments*, vol. 63, no. 10, pp. 5140–5147, 1992.

[35] C. T. Holcomb, M. A. Makowski, S. L. Allen, W. H. Meyer, and M. A. \mboxVan Zeeland, "Overview of equilibrium reconstruction on \mbox{DIII-D} using new measurements from an expanded motional \mbox{Stark} effect diagnostic," *Rev. Sci. Instrum.*, vol. 79, p. 10F518, 2008.

[36] H. S. T. John, "Equations and Associated Definitions Used in Onetwo," 2005.

[37] O. Sauter, C. Angioni, and Y. R. Lin-Liu, "Neoclassical conductivity and bootstrap current formulas for general axisymmetric equilibria and arbitrary collisionality regime," *Phys. Plasmas*, vol. 6, p. 2834, 1999.

[38] O. Sauter, C. Angioni, and Y. R. Lin-Liu, "Erratum: Neoclassical conductivity and bootstrap current formulas for general axisymmetric equilibria and arbitrary collisionality regime (Physics of Plasmas (1999) 6 (2834))," *Physics of Plasmas*, vol. 9, no. 12, p. 5140, 2002.

Appendix A

CAKE settings

Below the standard settings for CAKE can be found. Three tables are depicted, starting with ELM detection and initial data sanitation. The parameters for the ELM filters are shown and the maximum acceptable errors on Thomson scattering and CER data. Next the fitting and parameter constraints are shown. Here the type of fits used and the minimum error are among the things displayed. Finally assumptions used in the calculation and the values are displayed. These results are automatically obtained from CAKE after a run is completed. The shot that has been used to generate the table is 172019 at 3580ms.

Setting	Default Value	Description
Assumptions for filling in incomplete datasets		
Assumptions for estimating thermal ions		
T_i/T_e	1.5	Ratio of ion to electron temperature
$n_{e,C}/n_e$	0.1	Fraction of electron density due to carbon
$C_{\sigma,ion}$	4.0	Uncert. multiplier for est. therm. ions
C_{edge,p_i}	1.5	Multiplier for p_i at edge
$\psi_{N,edge,p_i}$	0.93	Definition of “edge” for C_{edge,p_i}
Assumptions for estimating fast ions		
T_{fast}	75.0 keV	Fast ion temperature
$\sigma_{T_{fast}}$	6.0 keV	Uncertainty in fast ion temperature
p_{fast}/p_e	0.3	Fast ion pressure as fraction of p_e
$\sigma_{p_{fast}}/p_e$	0.3	Fast ion pressure uncert. as fraction of p_e
$C_{fast,NBI}$	0.1	p_{fast} enhancement factor for NBI

Table A.1: Assumptions setup for CAKE

Setting	Default Value	Description
ELM processing		
ELM detection		
F_{smo}	butter_smooth	Smoothing function
τ_1	0.50 ms	Timescale for mild smooth
$F_{\tau 2}$	5.00	Factor for determining heavy smooth ($F_{\tau 2} = \tau_2/\tau_1$)
$F_{\tau d1}$	0.00	Factor for determining mild smooth for derivative from τ_1
$F_{\tau d2}$	4.00	Factor for determining heavy smooth for derivative from τ_1
DS_{lim}	0.05	Threshold on difference of smooths normalized to max.
DD_{lim}^{+}	0.14	Threshold on difference of smooth derivs. when $DD > 0$
DD_{lim}^{-}	0.14	Threshold on difference of smooth derivs. when $DD < 0$
$f_{DD,lim}$	1.00	Multiplier for $DD_{lim}^{\pm}$ when $DS < 0$
b	7.00 samples	Averaging neighborhood width for debouncing
ELM filtering		
$\phi_{ELM,min}$	0.00	Minimum ELM phase
$\phi_{ELM,max}$	1.00	Maximum ELM phase
$t_{ELM,accept}$	25.00 ms	Delay after ELM ends before accepting data regardless of phase
$t_{ELM,reject}$	0.10 ms	Period after ELM ends when data are rejected regardless of phase
Initial data sanitization		
Thomson scattering		
$\chi^2_{red,max}$	8.00	Max. acceptable reduced χ^2
$(\sigma_{Te}/T_e)_{\max}$	0.50	Max. acceptable fractional uncertainty in T_e
$(\sigma_{Te}/T_e)_{cold,\max}$	0.95	Max. acceptable fractional uncertainty in T_e at low T_e
$T_{e,cold}$	50.00 eV	Threshold for using cold limit on σ_{Te}/T_e
$(\sigma_{ne}/n_e)_{\max}$	0.50	Max. acceptable fractional uncertainty in n_e
CER		
$(\sigma_{Ti}/T_i)_{\max}$	0.11	Max. acceptable fractional uncertainty in T_i
$(\sigma_{nC}/n_C)_{\max}$	0.25	Max. acceptable fractional uncertainty in n_C

Table A.2: Input filtering settings for CAKE

Setting	Default Value	Description
Profile fitting		
Fitting functions		
F_{Te}	lmfit_tanh_then_mod	Function to use for fitting T_e
F_{ne}	lmfit_asym_tanh_then_mod	Function to use for fitting n_e
F_{Ti}	basic_monte_carlo_spline	Function to use for fitting T_i
F_{fz}	basic_monte_carlo_spline	Function to use for fitting f_z
Sanitization of uncertainties in fit inputs		
$\sigma_{min,Te,fit}$	1.00 eV	Min. uncertainty for input when fitting T_e
$\sigma_{min,ne,fit}$	1E+18 m^{-3}	Min. uncertainty for input when fitting n_e
$\sigma_{min,fz,fit}$	0.01	Min. uncertainty for input when fitting f_z
Miscellaneous profile fitting settings		
S_{ne}	1E-19	Scaling factor for density measurements before fitting
S_{other}	1.00	Scaling factor for other measurements before fitting
Constraint setup		
Pressure constraint		
$\sigma_{min,pe,frac}$	0.02	Min. fractional uncertainty in p_e term in constraint
$\sigma_{min,pe}$	100.00 Pa	Min. absolute uncertainty in p_e term in constraint
n_{pc}	200	Number of pressure constraint points
$\langle\psi_{pc}\rangle$	0.50	Average ψ_N position of pressure constraint points
$\psi_{pc,min}$	0.00	ψ_N position of innermost pressure constraint point
$\psi_{pc,max}$	1.00	ψ_N position of outermost pressure constraint point
Current constraint		
n_{cc}	31	Number of current constraint points
$\langle\psi_{cc}\rangle$	0.86	Average ψ_N position of current constraint points
$\psi_{cc,min}$	0.50	ψ_N position of innermost current constraint point
$\psi_{cc,max}$	1.00	ψ_N position of outermost current constraint point
Miscellaneous constraint settings		
$\sigma_{OT,frac}$	0.20	Fractional error, fast ion results from ONETWO

Table A.3: Default tuning for CAKE

Appendix B

DCON settings

DCON, used as part from the GPEC-tools, as dozens of variable that can be chosen. However, most of them are already filled in for standard scenarios. Below is a table with variables that are picked or important parameters that are standardized but important for the reproducibility of the results that have been obtained in this work .

Setting	Default Value	Description
DCON settings		
nn	1	Toroidal mode number
jac_type	'hamada'	Jacobian that has been used
psilow	0.001	Minimum value of ψ_n
psihigh	0.992	Maximum value of ψ_n
sas_flag	True	Truncate if the last calculated value is at a rational surface
a	0.2	Distance from plasma to wall in meter.

Table B.1: Input settings for DCON

Appendix C

Results Unscented Transform

This appendix contains the result from the 10 unscented transforms to determine the standard deviation of δW.

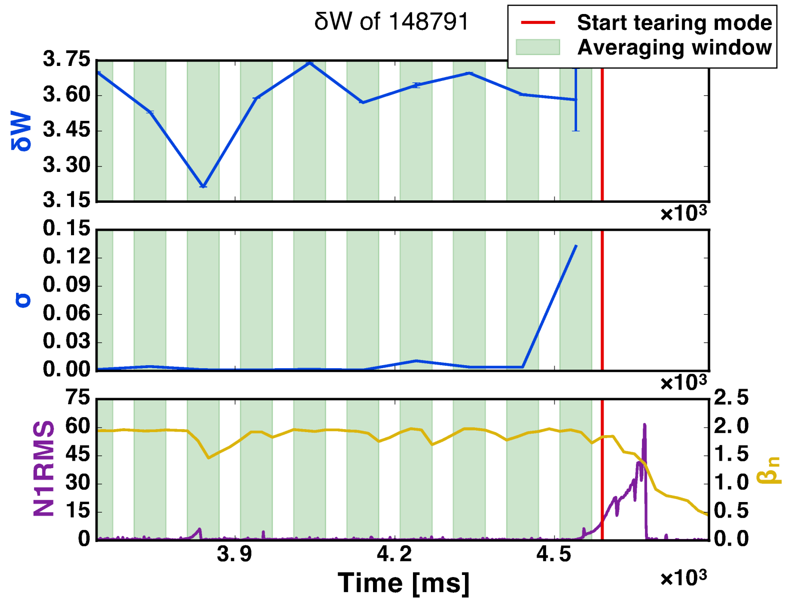

Figure C.1: Unscented transform for discharge 148791

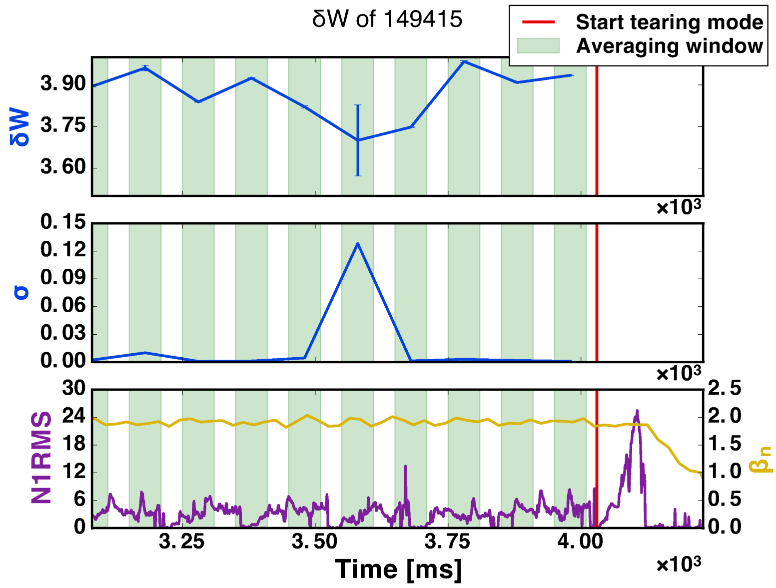

Figure C.2: Unscented transform for discharge 149415

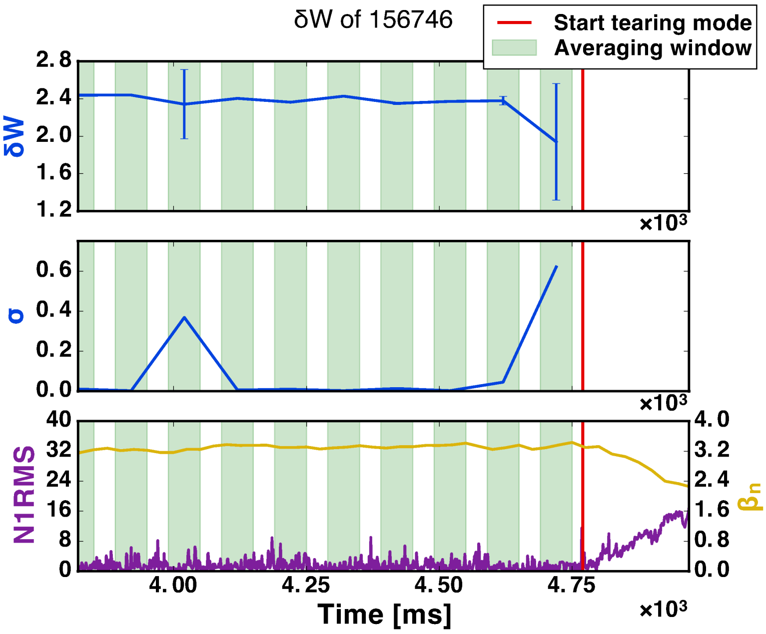

Figure C.3: Unscented transform for discharge 156746

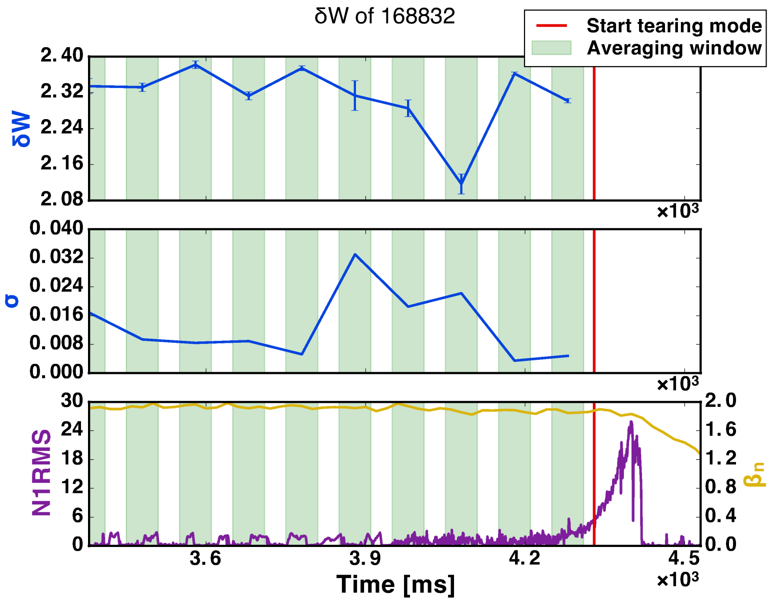

Figure C.4: Unscented transform for discharge 168832

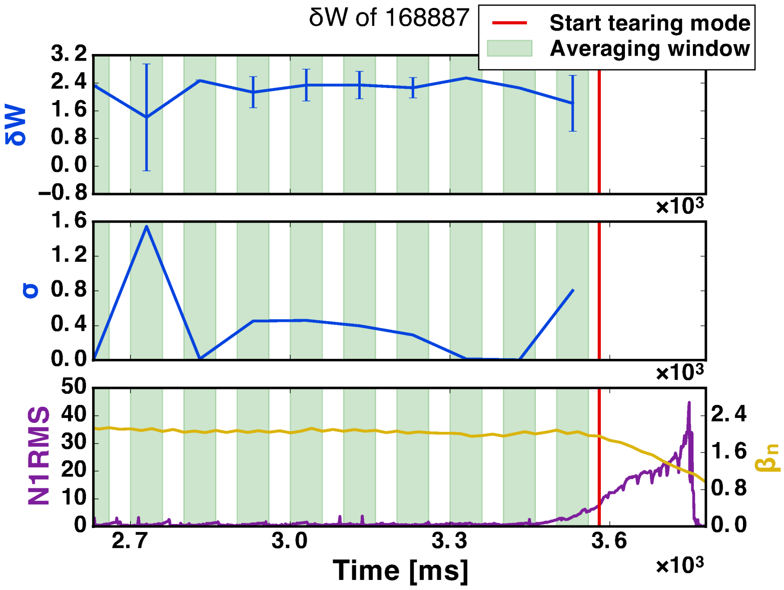

Figure C.5: Unscented transform for discharge 168887

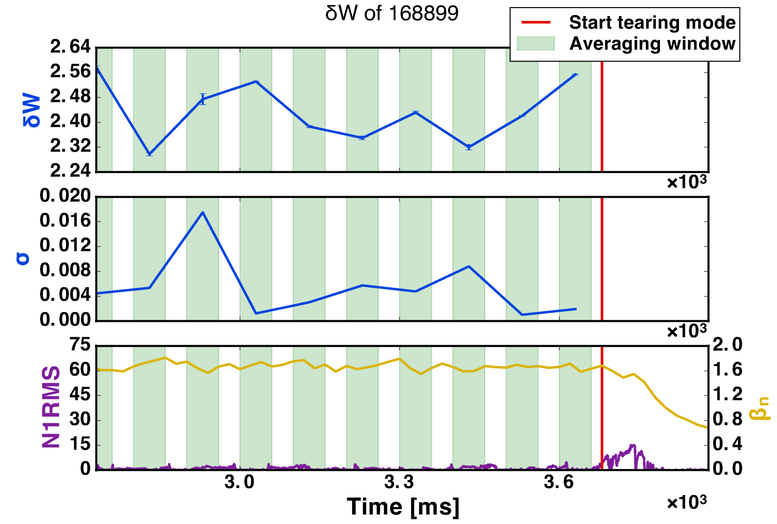

Figure C.6: Unscented transform for discharge 168899

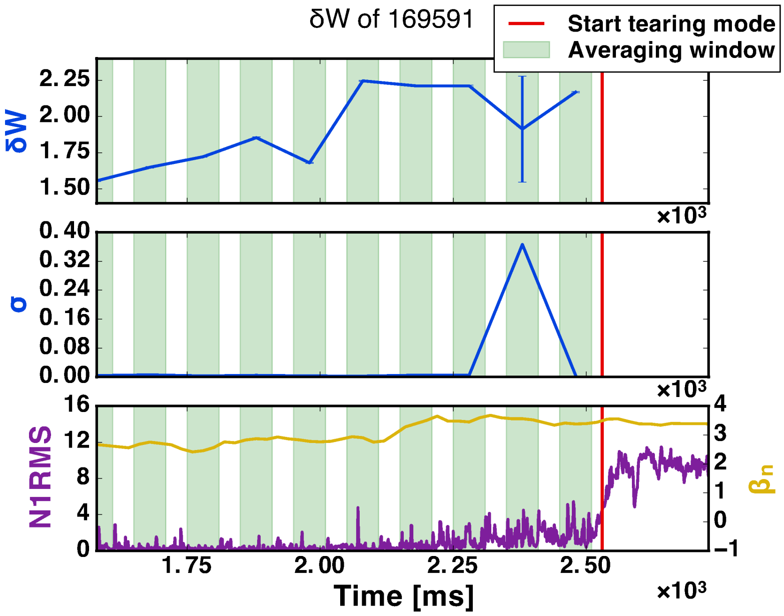

Figure C.7: Unscented transform for discharge 169591

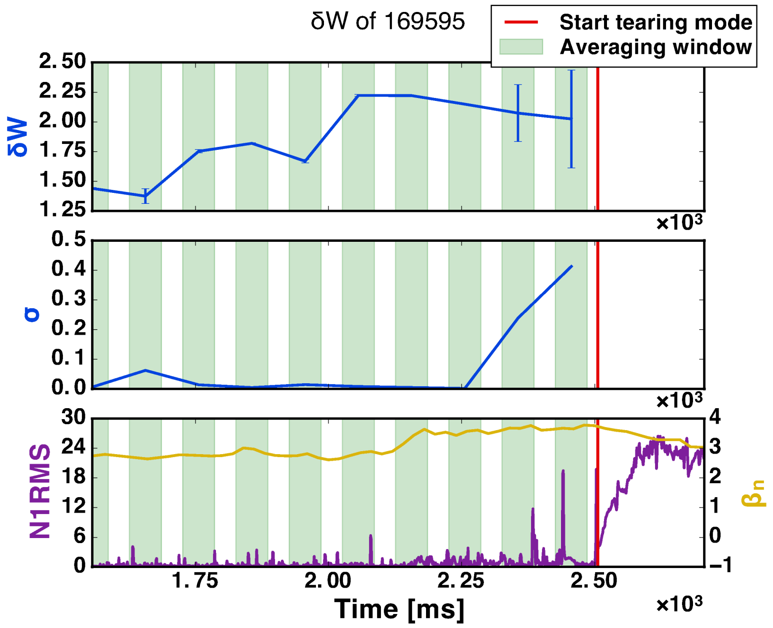

Figure C.8: Unscented transform for discharge 169595

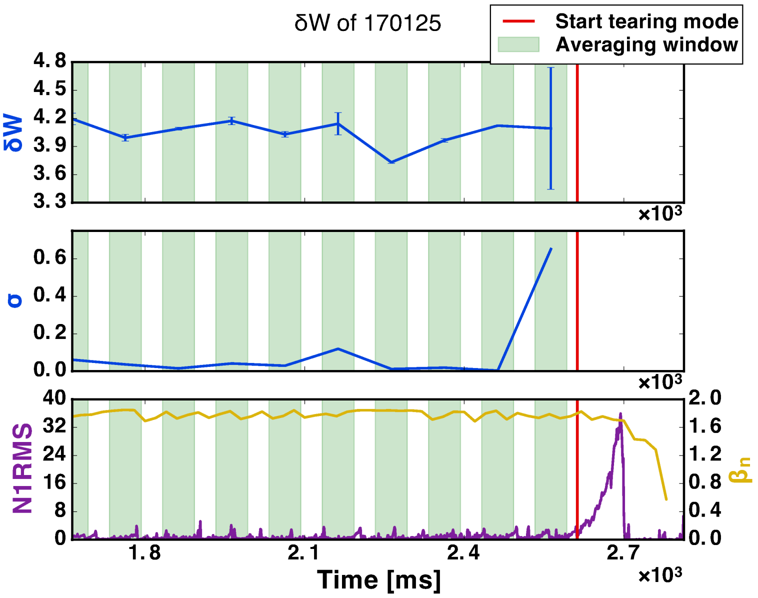

Figure C.9: Unscented transform for discharge 170125

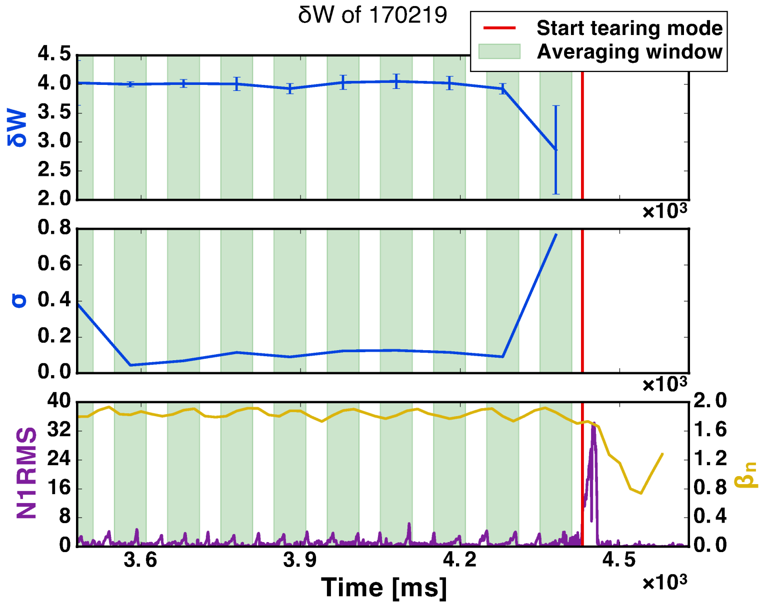

Figure C.10: Unscented transform for discharge 170219